Anisotropic Cellular Mechanoresponse for Radial Size Maintenance of Developing Epithelial Tubes

Tsuyoshi Hirashima*[1] and Taiji Adachi[2]

1. Department of Pathology and Biology of Diseases, Graduate School of Medicine, Kyoto University
2. Institute for Frontier Life and Medical Sciences, Kyoto University

Correspondence to:

Tsuyoshi Hirashima, Ph.D.

Department of Pathology and Biology of Diseases, Graduate School of Medicine, Kyoto University, Yoshida-konoe-cho, Sakyo-ku, Kyoto 606-8315, Japan.

Tel/Fax: +81-75-753-9450

E-mail: hirashima.tsuyoshi.2m@kyoto-u.ac.jp

Abstract

Cellular behaviors responding to mechanical forces control the size of multicellular tissues as demonstrated in isotropic size maintenance of developing tissues. However, how mechanoresponse systems work to maintain anisotropic tissue size including tube radial size remains unknown. Here we reveal the system underlying radial size maintenance of the murine epididymal tubule by combining quantitative imaging, mathematical modeling, and mechanical perturbations. We found that an oriented cell intercalation making the tubule radial size smaller counteracts a cell tension reduction due to neighbor cell division along the tubule circumferential axis. Moreover, we demonstrated that the tubule cells enhance actomyosin constriction driving the cell intercalation in response to mechanical forces anisotropically applied on the cells. Our results suggest that epididymal tubule cells have endogenous systems for responding as active cell movement to mechanical forces exclusively along the circumferential axis, and the anisotropic cellular mechanoresponse spontaneously controls the tubule radial size.

Keywords: Epididymal tube, Mechanoresponse; Multiphoton live imaging; Vertex model, Size regulation

Introduction

Cell-cell communication via cellular behaviors is necessary to regulate homeostasis including size maintenance in development. The underlying principle for this communication is a cellular response in reaction to mechanical forces generated within the tissues (Guillot and Lecuit, 2013; Mammoto et al., 2013). In tissue volume maintenance, for example, cell proliferation is counterbalanced by cell death, and these coordinated cellular behaviors are invoked in response to cell-crowding pressure generated by cell proliferation as a mechanoresponse (Eisenhoffer et al., 2012; Gudipaty et al., 2017; Hufnagel et al., 2007; Shraiman, 2005). On the other hand, in tissue length maintenance along an axis, such as radial size maintenance of tubes during elongation (Andrew and Ewald, 2010; Hirashima, 2014; Karner et al., 2009), anisotropic mechanoresponse systems in tissues might organize cooperative cellular behaviors to distribute a net increase in the tissue volume not along the axis but in the other axes.

The length maintenance in developing tissues can be considered as another aspect of anisotropic tissue growth giving rise to a variety of tissue shape (Thompson, 1942). Recent studies have revealed so far that mainly two factors at cellular level underpin the anisotropic tissue growth. One is cell division orientation, determined by the position of the mitotic spindle. It has been shown that the shape of growing tissues largely obeys the orientation of cell division, and also increasing evidence implicates the misorientation of cell division leads to the abnormal morphology in tissues as demonstrated in various organs and species (Fischer et al., 2006; Morin and Bellaïche, 2011; Tang et al., 2011). The other one is cell intercalation, active cellular movement with changing the position of cell junctions in neighboring cells (Guillot and Lecuit, 2013; Walck-Shannon and Hardin, 2014). It has been clearly demonstrated that the cell intercalation is driven by polarized myosin II localization at cell-cell junctions and cumulative effect of the local tissue dynamics results in anisotropic

large deformation at the tissue scale (Bertet et al., 2004; Nishimura et al., 2012; Zallen and Blankenship, 2008). These cellular events generate mechanical forces and thereby impact on surrounding cells in multicellular packing tissues, suggesting a mechanoresponse system interconnecting constituent cells would be formed in developing tissues. However, it remains unclear how the system works to be responsible for the tissue length maintenance in the dynamics.

Here we utilized epididymal tubules in murine embryo as an experimental model system to reveal anisotropic cellular responses to mechanical forces. The epididymal tubule is a single mono-layered epithelial tube that shows dynamic morphological change including bending and folding during the development from embryonic day (E) 15.5 (Hirashima, 2014; Hirashima, 2016; Joseph et al., 2009). Interestingly, the radial size of developing epididymal tubule is almost constant even though the tissue volume increases due to incessant cell proliferation in the tubules (Hirashima, 2014; Hirashima and Adachi, 2015; Tomaszewski et al., 2007). To reveal the mechanism to explain this phenomenon, Xu et al. have shown that the oriented cell intercalation is involved in the tubule elongation with maintaining the radial size (Xu et al., 2016). If the oriented cell intercalation have sustained in the epididymal tubule, the radial size would become smaller along the time during the development, inconsistent with the observation. Therefore, this study motivates us to unravel unknown regulations for the radial size maintenance of epididymal tubules. In this paper, we employed interdisciplinary approach combining quantitative imaging and mathematical approaches, and found that the epididymal cells counteract mechanical forces exclusively along the circumferential axis of tubule. We finally propose the anisotropic mechanoresponse system at supra-cellular scales that operates to maintain the tubule radial size at whole tissue scale.

85 # Results

86 **Non-oriented cell division produces mechanical forces to expand the tubule**

87 Since the cell division orientation has been known as a key determinant for the
88 morphogenesis of developing tubes (Fischer et al., 2006; Tang et al., 2011), we examined the
89 impact of cell division orientation in the tubule at E15.5 and E16.5. We first performed
90 immunostaining for phospho-histon H3 (pHH3) and γ-tubulin each as a marker of mitotic
91 cells and microtubule organizing centers (MTOCs), and marked spindle orientation in the
92 mitotic cells within the tubule by extracting the axis connecting between the two MTOCs in
93 each pHH3-positive cell without destructing the tissue structure (Fig. 1A-A′′). Then, we
94 manually measured three angles α_1 , α_2, and α_3 (Fig. 1B) to define a local coordinate system
95 *O*' (Fig. 1C), origin of which corresponds to the center position of mitotic cell (white arrows
96 in Fig. 1B). In the local sphere coordinates, we obtained statistical distributions for two
97 angles of the cell division orientation: φ and θ (Fig. 1C; Materials and Methods (II-i)).
98 The distribution of φ shows that most of the mitotic cells divide parallel to the epithelial
99 layer (The Rayleigh test, $P<0.001$ at E15.5 and E16.5); however, the distribution of θ
100 shows that the cell division orientation is not biased towards the longitudinal or
101 circumferential axis (The Rayleigh test, $P>0.05$ at E15.5 and E16.5) (Fig. 1D). Furthermore,
102 the distance between MTOCs shows no correlations with the angle θ (r=-0.07 at E15.5,
103 r=-0.02 at E16.5 where r is the Pearson's correlation coefficient) (Fig. 1E), rejecting that the
104 spindle orientation might turn to a specific orientation in the later stage of mitosis.

105 We then investigated how the cell division orientation affects the tubule morphology
106 using numerical simulations of a computational model (Mov. 1). We here employed the
107 vertex dynamics model, a type of cell-oriented model, to represent multi-cellular dynamics in
108 epithelial tubes (Fletcher et al., 2014; Nagai and Honda, 2001; Rauzi et al., 2008). See the
109 Materials and Methods (III-i) - (III-iii) for more details of the mathematical model and

110 simulation settings (Fig. S1). In the simulation, virtual epithelial tubes grew along the
111 division orientation, indicating that cell division along the circumferential axis is attributed to
112 continuous radial growth (Fig. 1F and F′). In addition, we found that the cell division
113 orientation affects mechanical stress in each cell of the virtual tubes (Fig. 1F). To evaluate the
114 mechanical stress in the tube cells, we introduced a scalar quantity, i.e., cell tension
115 anisotropy, which becomes larger when the cell tension along the circumferential axis
116 becomes weaker than that along the longitudinal axis. See Eq. (iv-2) in the Materials and
117 Methods (III-iv) for the definition of cell tension anisotropy. As shown in Figure 1F-F′′, the
118 cell tension anisotropy in the tubes depends on the cell division orientation and corresponds
119 with the growth direction of the tubes. The simulation analysis indicates that the
120 circumferential cell division entails the increase of cell tension anisotropy locally in the tissue,
121 resulting in the tube expansion. This implies that cells should actively counteract the changes
122 in cell tension anisotropy for the maintenance of tubule radial size.
123
124 **Polarized actomyosin constriction generated in the tubule cells suppresses the tubule**
125 **expansion**
126 To study how the cells react against the circumferential cell division, we focused on
127 phosphorylated myosin regulatory light chain (pMRLC), a marker of active tension
128 generation via actomyosin constriction. We first examined the localization of pMRLC in the
129 epididymis by whole-tissue co-immunostaining for the pMRLC and an apical tight junction
130 marker Zonula occludens-1 (ZO-1). The immunostainings revealed that the pMRLC localizes
131 only at apical cellular junctions of the epithelial tubules at E15.5 and E16.5 (Fig. 2A).
132 Furthermore, the pMRLC localization is polarized along the circumferential axis of the
133 tubules (Fig. 2A).
134 For quantification of the pMRLC spatial distribution at sub-cellular resolution, we

135 measured the pMRLC mean intensity at junctions, junction angle ϑ, and junction length ℓ
136 through automatic extraction for each apical cell junction by digital image processing (Fig.
137 2B and C; Materials and Methods (II-ii)). The distribution of pMRLC intensity was well
138 fitted to the heavy-tails of log-normal distribution (Fig. 2D), indicating that enriched pMRLC
139 localizations can be observed in an unignorable number of apical junctions instead of random
140 fluctuations. This statistical distribution suggests that the myosin would be able to be
141 activated by biological events that occur intermittently with low frequency rather by constant
142 regulation. To evaluate the relationship between the junction angle and the pMRLC intensity,
143 we categorized the junction angle into three groups; longitudinal (long.): $0 \le \vartheta \le \pi/6$,
144 intermediate (intm.): $\pi/6 < \vartheta < \pi/3$, and circumferential (circ.): $\pi/3 \le \vartheta \le \pi/2$ (Fig. 2E). As
145 shown in Figure 2E′, the pMRLC tends to localize more on junctions that orient more in the
146 circumferential axis (One-way ANOVA, $P<0.001$). The variation in the position of pMRLC
147 distribution between the junction angles does not show huge difference but reflects that the
148 myosin activation depends on rare events rather than regulations driving large deformation of
149 epithelial tissues such as fly wing or neural tubes. As well as the junction angle, we also
150 categorized the junction length into three groups: short: $0 \le \ell \le 2$ μm, middle: $2 < \ell < 4$ μm,
151 long: $4 \le \ell \le 10$ μm (Fig. 2F), and found that the pMRLC tends to localize more on shorter
152 junctions (One-way ANOVA, $P<0.001$) (Fig. 2F′). These quantifications suggest that the
153 polarized actomyosin-mediated constriction would shrink the circumferential apical
154 junctions.

155 We then examined the mechanical roles of actomyosin constriction for the tubule
156 morphology in the inhibitor assay. We applied Blebbistatin/Y-27632 for inhibiting
157 actomyosin constriction by non-muscle myosin II (Kovács et al., 2004; Watanabe et al.,
158 2007) to the epididymides in explant cultures, and observed the tubule morphology 1 day
159 after the inhibitor treatment. The assay revealed that inhibiting actomyosin-mediated apical

160 constriction resulted in the tubule expansion (One-way ANOVA, $P<0.001$) (Fig. 2G and G′;
161 Materials and Methods (II-iii)). In addition, we found that even when the inhibitors were
162 treated, the mitotic cells remain in the epididymal tubules to the same extent as the control
163 ones (Fig. 2H). Although the inhibitor treatment might impede the cytokinesis, the
164 epididymal tubule cells could enter the M phase in the cell cycle. Hence, the inhibiting
165 actomyosin constriction affects little the change in local tissue volume within 1 day. These
166 results indicate that the active constriction polarized circumferentially at the apical junction
167 of epididymal tubules is required for the maintenance of tubule radial size.
168
169 **Cell division should trigger the polarized myosin activation for the maintenance of**
170 **tubule radial size**
171 It has been clarified that the polarized pMRLC localization drives cell intercalation mediated
172 through junction shrinkage in the developing epididymis (Xu et al., 2016) as well as shown in
173 other contexts (Andrew and Ewald, 2010; Guillot and Lecuit, 2013; Walck-Shannon and
174 Hardin, 2014). Hence, the polarized pMRLC localization on the circumferential junctions can
175 drive the oriented cell intercalation, eventually leading to longitudinal elongation and radial
176 shrinkage of the tubule (Bertet et al., 2004; Honda et al., 2008). In contrast, non-oriented cell
177 proliferation results in the tubule expansion as shown in the earlier section. Therefore, the
178 maintenance of tubule radial size requires a proper balance between myosin activity driving
179 intercalation and cell proliferation frequency.
180 To evaluate this relationship, we measured the pMRLC intensity along the tubule at the
181 whole organ scale at E15.5 and E16.5 (Materials and Methods (II-iv)), and found that the
182 intensity in the head region of epididymis is larger than that in the tail region (Fig. 3A). This
183 intensity profile is similar to the spatial profile of the mitotic cell number in the epididymal
184 tubules previously reported (Hirashima and Adachi, 2015) (Fig. 3B). Indeed, the pMRLC

185 intensity and the mitotic cell numbers in the tubules show positive correlation (r=0.49 at
186 E15.5 and r=0.56 at E16.5 where r is the Pearson's correlation coefficient) (Fig. 3B and B′;
187 Materials and Methods (II-v)). Western blotting analysis also shows the myosin activity,
188 defined as the ratio of pMRLC to the total MRLC (tMRLC), in the head region is greater than
189 that in the tail region (Fig. 3C and C′). Moreover, cell morphology differences corroborate
190 junctional tension due to the pMRLC in each region (Fig. 3D and S2; Materials and Methods
191 (II-vi)). The apical junction length along the circumferential axis in the head region is shorter
192 than that in the tail region (Kruskal-Wallis test, P<0.001) (Fig. 3D′), and the apical surface
193 area in the head region are smaller than that in the tail region (Kruskal-Wallis test, P<0.001)
194 (Fig. 3D′′).
195 Although there are positive correlations between the myosin activity and mitotic cell
196 number in the tubule, the cell proliferation is of no significant dependence on the myosin
197 activity because the inhibition of myosin activity does not affect the mitotic cell number.
198 Thus, it is reasonable to consider that the myosin activation is triggered by the cell
199 proliferation to achieve the balance for the radial size maintenance.
200
201 **Cell division yields mechanical stimulations to the neighboring cells**
202 To explore how the cell proliferation triggers the myosin activation, we examined the
203 mechanical effects of cell proliferation in the tubules using the vertex dynamics model. It has
204 been shown that the cell division can produce mechanical perturbations in multi-cellular
205 tissues (Stewart et al., 2011); hence, we anticipated that the cell division apply the pushing
206 forces to the neighbors of divided cells and this stimulus would trigger the polarized myosin
207 activation in the pushed cells. We investigated the change of the cell tension anisotropy
208 against the cell division in the extensive numerical analysis.

209 We first examined how the cell division affects the cell tension anisotropy in the
210 neighbors of divided cells. To do so, we noticed each spatial and temporal factors: relative
211 angle of target cells to the cell division axis (Fig. 4A) and normalized elapsed time from the
212 cell division $\tau_{\alpha}^{\prime\mathrm{cycle}}$, ranged from 0 to 1 (see the Materials and Methods (III-iii) for the
213 definition). We then evaluated the distribution of cell tension anisotropy in the two cases of
214 cell division orientations, i.e., longitudinal ($0 \le \theta \le \pi/6$ where θ is defined in Fig. 1C) and
215 circumferential ($\pi/3 \le \theta \le \pi/2$) (Fig. 4B). The results shown in Figure 4B′ indicate that the
216 smaller the relative angle, the larger the cell tension anisotropy in the neighbors of divided
217 cells can be altered (upper rows in Fig. 4B′). Note that small relative angle means that the
218 measured cells are located to the circumferential direction of divided cells for the
219 circumferential cell divisions while ones are located to the longitudinal direction of divided
220 cells for the longitudinal cell divisions. This result is intuitive because the divided cells push
221 along the division axis to the neighboring cells, and hence, tension in the neighboring cells
222 along the division axis can be attenuated. In addition, the histograms clearly show that the
223 tension attenuation due to the cell division is the most significant soon after the cell division
224 (the leftmost column in Fig. 4B′) and becomes smaller along with the elapsed time from the
225 cell division $\tau_{\alpha}^{\prime\mathrm{cycle}}$.

226 We then examined the time-dependency of change in the cell tension anisotropy from
227 the cell division. In so doing, we monitored cell tension anisotropy ρ_{α} in all cells, and
228 marked cells as the target cells when ρ_{α} was over various thresholds ρ^*. Then, we
229 counted the elapsed time from the cell division $\tau_{\alpha}^{\prime\mathrm{cycle}}$ in the neighboring cells located on the
230 circumferential axis from the target cells, since we have focused on the circumferential cell
231 division that conduces to the tubule expansion. We here set the thresholds as
232 $\rho^* = 0.039,\ 1,$ and 0.2 ($\rho^* = 0.039$ is the mean of cell tension anisotropy in the upper-left

233 case of Fig. 4B′) (Fig. 4C-C′′). Our numerical investigations revealed that the cell tension
234 anisotropy in most of the cells (~70%) was altered immediately following to the cell division,
235 consistent with the results of the previous analysis (Fig. 4B′). In addition, we found that the
236 cell tension anisotropy could become over the given thresholds at timing elapsed enough
237 from the cell division (small windows in Fig. 4C-C′′). This occurs because anisotropic
238 deformation of individual cells can be induced by the mechanical stress accumulated in the
239 local regions owing to non-adjacent cell proliferation instead of adjacent cell proliferation.
240 These analyses provided the two suggestions. First, most of the cells that receive
241 significant mechanical impact from the neighboring divided cells can be found soon after the
242 cell division. Second, cell tension can be varied independent to the cell division, rationalizing
243 the introduction of mechano-responsive regime into our model argued in the later section.
244

245 **Mechanical stimulations provided by neighbor cell divisions trigger the onset of cell**
246 **intercalation**

247 To directly observe cellular responses to the mechanical forces generated by the cell divisions,
248 we performed live imaging analysis for epididymal tubule cells dissected at E15.5 using ex
249 vivo organ culture systems. For visualization of the tubule cell membrane, we crossed the
250 R26R-Lyn-Venus line (Abe et al., 2011) and the Pax2-Cre line (Ohyama and Groves, 2004)
251 to create a conditional fluorescence reporter line. Because the epididymal tubules were
252 located in deep region of the epididymis, ~100 μm away from the capsule of epididymides
253 (Fig. 5A), confocal microscopy was not appropriate for this case; hence, we employed an
254 incubator-integrated multiphoton excitation microscope system for stable deep tissue live
255 imaging in explant cultures (Fig. 5B).
256 We focused on the behavior of cells neighboring to mitotic cells on the cell division axis
257 as those cells are more likely to show cellular responses against the mechanical perturbations

258 according to the first suggestion in the previous section. Careful observations led to the
259 discovery of characteristic behaviors in those cells; the oriented cell intercalation for
260 elongating the tubule occurs more frequently against the circumferential cell division
261 compared against the longitudinal one (Fig. 5C and Mov. 2). For quantification of the
262 oriented cell intercalation behavior, we measured the cell intercalation strain rate (Blanchard
263 et al., 2009) for the circumferential ($0 \le \theta \le \pi/6$) or longitudinal cell division
264 ($\pi/3 \le \theta \le \pi/2$) (Fig. 5C and S3), and calculated the cell intercalation rate for tube
265 elongation (CITE) as a measure of the oriented cell intercalation in the tubules.
266 Positive/negative values of the CITE indicate that cell intercalations undergo for the tubule
267 elongation/shortening (Fig. 5D; see the Materials and Methods (II-vii) for more details of
268 CITE). From the quantitative analysis, we found that the oriented cell intercalation tends to
269 occur 60 min after the circumferential cell division (*t*-test $P<0.05$ in the time range: 50-60
270 min in the case of circumferential cell division) (Fig. 5E).

271 Considering the cellular movement as an output response, the oriented cell intercalation
272 should be operated through rapid biochemical process such as phosphorylation. In addition to
273 this inference, we demonstrated by the extensive numerical simulations that the cell division
274 within the epithelial tissues could attenuate the cell tension in adjacent cells along the
275 division orientation owing to pressure of the dividing cells to the adjacent ones (Fig. 1F and
276 4B´). Therefore, we hypothesized that MRLC would be phosphorylated as a cellular response
277 to the reduction of circumferential cell tension provided by the neighboring cells, ultimately
278 driving the oriented cell intercalation.

279

280 **Polarized cellular responses to mechanical simulations lead to the maintenance of the**
281 **tubule radial size**

282 To check whether this hypothesis is rational, we carried out the computer simulation of the

283 vertex dynamics model including a mechano-responsive regime and its counterpart regimes
284 (Mov. 3). We implemented the mechano-responsive regime into the mathematical model as
285 the cells keep constricting one of the circumferential junctions for a parameterized period
286 since the cell tension anisotropy ρ_α reached at the threshold value ρ^* due to the reception
287 of intense pressure (Fig. 6A and S4; Materials and Methods (III-iv)). The numerical
288 simulation of the model clearly suggests that the mechano-responsive regime can realize
289 spatiotemporally-constant tubes with smaller radial size compared to the case of no
290 regulation (Fig. 6B and D).

291 On the other hand, we performed simulations in a counterpart regime, the 'scheduled'
292 regime, where the timing for junction constriction was predetermined and the constricting
293 cells were randomly selected. For determining the schedule of the constriction, we sampled
294 the ratio of constricting cells along the normalized simulation time τ' in the
295 mechano-responsive regime and obtained the function by fitting the mean curve data (Fig.
296 6C; see Eq. (iv-3) in the Materials and Methods (III-iv)). In the scheduled regime, the tubes
297 can be formed with irregular surfaces and non-constant radial size along the longitudinal axis
298 whereas the radial size was smaller than no regulation as well as the case of
299 mechano-responsive regime (Fig. 6B, D and D´).

300 In the scheduled regime, the oriented cell intercalation that leads to the local shrinkage
301 of tubules occurs independently to the variations of cell tension, resulting in the irregular
302 surface of tubules. In the mechano-responsive regime, however, the mechanical stress at the
303 supra-cellular scale can be modulated due to the active multicellular movement immediately
304 responding to the mechanical perturbations; therefore, the smooth-curved surface throughout
305 the longitudinal axis of tubules can be realized in this regime. These simulation analyses
306 suggest that the mechano-responsive regime, as an embodiment of our hypothesis, explain
307 the radial size maintenance of proliferating tubes.

308

309 **The epididymal tubule cells activate myosin in response to anisotropic mechanical**
310 **perturbations**

311 To verify the hypothesis, we applied uniaxial compression (~33%) to isolated epididymides
312 embedded in collagen gel using a flexible polydimethylsiloxane (PDMS) chamber, and
313 evaluated the myosin activity as a cellular response to the compression (Fig. 7A). We
314 performed the compression assay for 3 groups, i.e., no uniaxial compression as the control,
315 lateral, and longitudinal compression, to examine the cellular response to different
316 mechanical perturbations (Fig. 7B). After 10 min of continuous load, we quantified the cell
317 shape and configuration altered to the uniaxial compression. For the quantification, we
318 extracted the shape of epididymal cells from the immunofluorescence images for E-cadherin
319 (Fig. 7C), and calculated the aspect ratio and the major axis angle from best-fit ellipses of the
320 cell shapes. The shape and configuration of cells in the uniaxial compression treatments were
321 significantly different from those in the no uniaxial compression, confirming that the
322 epididymal tubule cells were deformed along the compression axis (The Kruskal-Wallis test,
323 $P<0.001$) (Fig. 7D-D′′).

324 After 20 min, we measured the myosin activity as the relative intensity of pMRLC to the
325 total MRLC (tMRLC) and found that the myosin activity is larger in the lateral compression
326 compared in other cases, indicating that the MRLC phosphorylation is exclusively enhanced
327 due to the lateral compression (The Friedman test, $P<0.05$) (Fig. 7E and E′). Moreover, we
328 quantified the level of MRLC kinase as the ratio of the Rho-associated protein kinase 1
329 (ROCK1) to the tMRLC, and found that it was not significantly different between treatments
330 (The Friedman test, $P>0.05$) (Fig. 7E and E′′). These results suggest that the epididymal
331 tubule cells possess an intrinsic system in which MRLC phosphorylation is triggered in
332 response to the cell tension reduction along the tubule circumferential axis without changing

333 the total amount of ROCK.

334

335 Discussion

336 Altogether, we showed that the cells trigger myosin activation leading to oriented cell
337 intercalation by responding to mechanical forces anisotropically in the tubule. Therefore, we
338 propose a system in which the mechanoresponsive behavior of cells at the supra-cellular scale
339 organizes the maintenance of the tubule radial size at the tissue scale (Fig. 4F). In
340 developmental processes, anisotropic growth of proliferating tissues while maintaining an
341 axis, such as tube elongation due to the radial maintenance specifically dealt with in this
342 study, causes generation of compressive forces in the growing axis, eventually leading to a
343 buckling-induced wavy pattern formation (Dong et al., 2014; Hirashima, 2014; Savin et al.,
344 2011). Thus, the proposed polarized mechanoresponse system might work as a regulatory
345 principle underlying mechanisms for self-organized tissue morphogenesis (Beloussov, 2015;
346 Sasai, 2013).

347 To understand the system further, future work will need to identify what molecular
348 machineries sense the anisotropic mechanical force in tissues and how the received
349 mechanical stimuli are chemically transduced to activate the myosin at apical junctions. It is
350 tempting to speculate that the directional preference of cells would be provided by regulators
351 of planar cell polarity (PCP) that promote the downstream myosin phosphorylation (Bosveld
352 et al., 2012; Guillot and Lecuit, 2013; Nishimura et al., 2012), such as Vang-like (VANGL)
353 and Tyrosine-protein kinase-like 7 (PTK7). These proteins are well aligned circumferentially
354 along junctions of epididymal tubule cells and loss of PCP disrupts the actomyosin-mediated
355 cell intercalation resulting in tubule expansion (Xu et al., 2016) (Fig. S5) as seen in renal tube
356 development (Karner et al., 2009; Kunimoto et al., 2017). Another possibility is that actin
357 filaments may function as polarity tension sensor in cooperation with unknown molecules

358 that specify the circumferential axis because those have been recognized to sense the tension
359 reduction (Galkin et al., 2012; Hayakawa et al., 2011). We believe that our findings move
360 forward to reveal structural components and dynamic properties in the polarized
361 mechanoresponse system that controls tissue morphogenesis.
362
363

364 # Materials and Methods

365 This section includes (I) Experiments, (II) Quantifications, (III) Mathematical modeling, and
366 (IV) Others (Statistical tests, etc.).

367

368 ## (I) Experiments

369 **(i) Animals**

370 For live imaging analysis, we used fluorescence reporter mice produced by crossing the
371 Pax2-Cre line(Ohyama and Groves, 2004) (a gift from T. Furukawa in Osaka Univ.) and
372 R26R-Lyn-Venus line(Abe et al., 2011). Otherwise, we used imprinting control region (ICR)
373 mice purchased from Japan SLC, Inc. We designated the midnight preceding the plug as
374 embryonic day 0.0 (E0.0), and all mice were sacrificed by cervical dislocation to minimize
375 suffering at E15.5 or E16.5. All the animal experiments were approved by the local Ethical
376 Committee for Animal Experimentation of Institute for Frontier Life and Medical Sciences,
377 Kyoto University, and were performed in compliance with the Guide for the Care and Use of
378 Laboratory Animals at Kyoto University.

379

380 **(ii) Antibodies and Fixative Solutions for Immunostaining**

381 We used the following primary antibodies with dilution ratio 1:200 as a standard condition:
382 rabbit monoclonal anti-E-cadherin (Cell Signaling Technology, #3195), mouse monoclonal
383 anti-γ-Tubulin, (Sigma-Aldrich, #5326), rabbit polyclonal anti-phospho histon H3
384 (pHH3)(Merck Millipore, #06-570), rat monoclonal anti-pHH3 (Abcam, #ab10543), rabbit
385 polyclonal anti-phosho Myosin light chain (pMRLC) (Abcam, #ab2480), rabbit polyclonal
386 anti-Vangl1 (Atlas Antibody, #HPA025235), goat polyclonal anti-Vangl2 (Santa Cruz
387 Biotechnology, #sc-46561), and mouse monoclonal anti-ZO-1 (Thermo Fischer Scientific,
388 #33-9100). We used the paraformaldehyde (PFA) for anti-E-cadherin, anti-γ-Tubulin, and

389 anti-pHH3; we used the trichloroacetic acid (TCA) for anti-pMRLC, anti-Vangl1,
390 anti-Vangl2, and anti-ZO-1.
391
392 **(iii) Whole-tissue Immunofluorescence and Fluorescent Dye**
393 Dissected epididymides were fixed with 4% PFA in phosphate buffered saline (PBS) for 2 h
394 at 4°C or for 20 min at 37°C, or with 2% TCA in Ca^{2+}- and Mg^{2+}-free PBS for 20 min at 4°C,
395 depending on target epitopes. The samples were then blocked by incubation in 10% normal
396 goat serum (NGS) (Abcam, #ab156046) or 10% normal donkey serum (Abcam, #ab166643)
397 diluted in 0.1% Triton X-100/PBS, depending on derived animals of secondary antibody, for
398 3 h at 37°C. The samples were treated with primary antibodies overnight at 4°C, and
399 subsequently incubated with secondary antibodies conjugated to either the AlexaFluor 546 or
400 the AlexaFluor 647 (1:1000, Thermo Fischer Scientific) overnight at 4°C. We used
401 TRITC-conjugated phalloidin (0.3 μg/ml, Merck Millipore, #FAK100) and Hoechst 33342 (5
402 μg/ml, Thermo Fischer Scientific, #H3570) for the visualization of F-actin and DNA,
403 respectively.
404
405 **(iv) Volumetric Fluorescence Imaging**
406 We mounted samples with 1% agarose gel of 10 μl on a glass-based dish (Greiner Bio-One,
407 #627871) for stable imaging. Then, the samples were immersed with the BABB solution
408 (benzyl-alcohol and benzyl-benzoate, 1:2) or CUBIC2 solution for optical
409 clearing(Hirashima and Adachi, 2015; Susaki et al., 2014; Yokomizo et al., 2012). Finally,
410 we obtained 8-bit volumetric fluorescence images using the confocal laser scanning platform
411 Leica TCS SP8 equipped with the hybrid detector Leica HyD. We used the objective lenses
412 magnifications of ×20 (numerical aperture (NA) = 0.75, working distance (WD) = 680 μm,
413 HC PL APO CS2, Leica), ×40 (NA = 1.3, WD = 240 μm, HC PL APO CS2, Leica), or ×60

414 (NA = 1.4, WD = 140 μm, HC PL APO CS2, Leica).

415

416 **(v) Explant Organ Culture**

417 The epididymides were surgically excised at a region of the vas deferens close to the tail of
418 epididymis, and those with testis were dissected from the embryonic body. Samples were
419 then placed on a hydrophilic polytetrafluoroethylene organ culture insert with a pore size of
420 0.4 μm (Merck Millipore, #PICM01250), which was preset in a 35 mm petri dish (Thermo
421 Fischer Scientific, #153066) filled with a culture medium. The culture medium we used was
422 Dulbecco's Modified Eagle's medium (Nacalai Tesque, #08489-45), containing 10% fetal
423 bovine serum (Thermo Fischer Scientific, #12483) and 1% penicillin-streptomycin mixed
424 solution (Nacalai Tesque, #26253-84) at 37°C under 5% CO_2. The samples were cultured in
425 an air-liquid interface; the total amount of culture medium was 800 μl for the petri dish.

426

427 **(vi) Small-molecule Inhibitors**

428 We used the following inhibitors to suppress or activate the generation of
429 actomyosin-mediated tension: Blebbistatin (Merck Millipore, #203391), Y-27632 (Merck
430 Millipore, #SCM075), and Calyculin A (Cell Signaling Technology, #9902).

431

432 **(vii) Live Imaging**

433 The organ culture setting was according to the condition as described above with the
434 following 2 minor modifications. First, we used a 35 mm glass-based dish (Iwaki,
435 #3910-035) with 700 μl of the culture medium in the dish. Second, we adhered each
436 supporting leg of the organ culture insert on the dish with 20 μl of 1% agarose gel. This
437 preparation prevents the culture insert from sliding during the live imaging. We used an
438 incubator-integrated multiphoton fluorescence microscope (Olympus) using a ×25

439 water-immersion lens (NA = 1.05, WD = 2mm, Olympus). Imaging conditions were as
440 follows; excitation wavelength: 945nm (Mai-Tai DeepSee eHP, Spectra-Physics), AOTF:
441 3.5%-1.5%, scan size: 1024 × 320 pixels, scan speed: 10 μsec/pixel, z-axis interval: 1 μm,
442 and time interval: 5 min, magnification: ×2.
443
444 **(viii) Tissue Compression Assay**
445 For the tissue compression assay, we used a manual stretch/compression device (STREX,
446 #STB-10) with a polydimethylsiloxane (PDMS) chamber (STREX, #STB-CH-04), and
447 conducted in the following manner. First, we exposed the PDMS chamber to plasma arc for 1
448 min using a desktop vacuum plasma processing device (STREX, PC-40) for hydrophilic
449 treatment to enhance the adhesion between the chamber and collagen gel into which the
450 epididymides were embedded. Next, we immediately placed isolated epididymides onto the
451 hydrophilized PDMS chamber in its 50% stretched state, and fulfilled with 500 μl of type I
452 collagen (Nitta Gelatin, Cellmatrix Type I-A), followed by gelation process for 10 min at
453 37°C. Then, we applied 1 ml of the culture medium into the chamber, and the epididymides
454 with the collagen gel were compressed by relaxing from the 50% stretched state around 0.2
455 mm/sec. No relaxing the stretched chamber was regarded as control treatment. Finally, the
456 samples were incubated for 10 min for the morphological confirmation analysis and 20 min
457 for the Western blotting analysis at 37°C under 5% CO_2. In the lateral compression assay, the
458 epididymal tubules were deformed along the circumferential axis in any peripheral region
459 and the circumferential length of individual cells became smaller. We consider this is due to
460 gravity of the culture medium filled on the upper layer of gel as this does not happen without
461 the culture media.
462 For the immunoblotting assay, we extracted total protein from each treatment, and
463 adjusted the amount to the same among the treatments for the SDS-PAGE as described above.

464 We first confirmed that there were no significant differences of GAPDH and those of MRLC
465 among the treatments. Then, we evaluated the myosin activity and the level of MRLC kinase
466 (ROCK1); even when the ROCK1 level in the epididymides was evaluated as the ratio of
467 ROCK1 to the GAPDH, it showed qualitatively the same results. There was no ROCK2
468 expression in the epididymides. Finally, the activities were each normalized by mean values
469 of the control group.
470
471 **(ix) Total Protein Extraction and Western Blotting**
472 For total protein extraction, dissected epididymides were immersed in the SDS-free RIPA
473 buffer with protease inhibitor cocktail (Nacalai Tesque, #08714) supplemented with the
474 EDTA-free phosphatase inhibitor cocktail (1:100, Nacalai Tesque, #07575), and were
475 disrupted by an ultrasonic cell disruptor (Microson). The lysates were placed onto the ice for
476 20 min and were centrifuged at 13,000 ×g for 10 min at 4°C. Protein concentration of the
477 supernatant was determined by the bicinchoninic acid assay.
478 The lysates were prepared for SDS-PAGE by adding 2×Laemmli sample buffer
479 (Bio-Rad, #161-0737) with 2-mercaptoethanol (Bio-Rad, #161-0710) and by boiling at 96°C
480 for 5 min. Next, the lysates containing approximately 5 μg of proteins were loaded into each
481 lane of the Mini-PROTEAN precast gels (Bio-Rad, #4569035), and electrophoresis was
482 carried out in Tris/glycine/SDS running buffer (Bio-Rad, #1610732) at constant 150V for 35
483 min. Then, the proteins were blotted onto 0.2 μm polyvinylidene difluoride membrane
484 (Bio-Rad, #1704272) in HIGH MW mode (1.3A, 25V for 10 min) of the Trans-Blot®
485 Turbo™ Transfer System (Bio-Rad, #170-4155) for ROCK1 detection and in the LOW MW
486 mode (1.3A, 25V for 5 min) for others.
487 The blotted membranes were then immersed in 15% H_2O_2/Tris-buffered saline (TBS)
488 solution for 30 min at room temperature for blocking endogenous peroxidase followed by

489 blocking with 5% NGS at 37°C for 60 min. For immunoblotting, the membranes were
490 incubated with primary antibodies diluted in 0.1% TBS/Tween-20 at 4°C over night. The
491 concentrations of antibodies used were 1:100,000 for mouse monoclonal anti-GAPDH (Wako,
492 #015-25473), 1:500 for rabbit polyclonal anti-myosin light chain 2 (Cell Signaling, #3672)
493 and mouse monoclonal anti-phospho-myosin light chain 2 (Cell Signaling, #3675), and
494 1:2000 for rabbit monoclonal anti-ROCK1 (Abcam, #ab45171). Then, the membranes were
495 incubated with diluted secondary antibody solutions in TBS/Tween-20 at 37°C for 60 min;
496 the concentration was 1:50,000 for goat anti-rabbit IgG conjugatd to horseradish peroxidase
497 (HRP) (Santa Cruz Biotechnology, sc-2004) and goat anti-mouse IgG conjugated to HRP
498 (Santa Cruz Biotechnology, sc-2005). Finally, protein bands were detected using the
499 Amersham ECL Select Western Blotting Detection Reagent (GE Healthcare, #RPN2235),
500 and were scanned with ImageQuant LAS 4000 (GE Healthcare).
501

502 ## (II) Quantifications

503 ### (i) Cell Division Orientation

504 We first performed coimmunolabeling for γ-Tubulin and pHH3 of 6 different epididymides
505 to detect microtubule organizing centers of mitotic cells as described in this section (I)-(iii)
506 with a minor modification. That is, the samples were incubated in 10 mM sodium citrate
507 buffer including 0.1% Triton X-100/PBS for 20 min at 80°C for heat-induced retrieval of
508 γ-Tubulin epitope before blocking treatment. Next, we obtained volumetric images of 1024 ×
509 256 pixels as described above using ×40 lens with z-axis interval of 1 μm. Third, we
510 manually measured three angles α_1, α_2, and α_3 shown in Fig. 2B for each mitotic cell to define
511 a local coordinate system (*O*'; see Fig. 2C), origin of which corresponds to the center position
512 of mitotic cell. Each orthogonal basis of *O*'-coordinate is defined as follows: longitudinal
513 direction of epididymal tubule (*x*'), surface normal of epididymal tubule (*z*'), and orthogonal

514 direction for both x' and z' according to the right-handed system (y'). Then, we manually
515 measured positions of the two γ-Tubulin-positive dots (microtubule organizing centers:
516 MTOCs) in a pHH3-positive cell, and obtained two angles φ and θ in a local sphere
517 coordinate (Fig. 2D) resulted from coordinate transformation into the O'-system. Finally, we
518 selected samples under a criterion that the distance between the two γ-Tubulin-positive dots
519 is more than 1.5 μm. We regarded the samples whose φ is less than 40 degree as cells
520 dividing in parallel to the surface of epididymal tubule.
521
522 **(ii) Apical Junction Morphology and pMRLC/VANGL Signal Intensity**
523 We performed coimmunostainining for ZO-1 and either pMRLC or VANGL2 of 8 different
524 epididymides as described above with a minor modification: the dilution ratio of
525 anti-pMRLC was 1:400 for preventing saturation binding. We obtained volumetric images of
526 1024 × 256 as described above using ×60 lens with z-axis interval of 0.3 μm. Then, we
527 separated the images into smaller ones around 200 pixels (≈36 μm) on a side so that the slope
528 of epididymal tubule can be regarded as a linear line.The longitudinal The digital image
529 processing was performed as follows. First, images for ZO-1 were filtered slice by slice with
530 a 2D median filter (3 × 3 pixels) followed by a 3D Gaussian filter with a standard deviation
531 of 3 pixels to reduce undesired noise. Next, the filtered images were binarized using the 3D
532 maximum entropy thresholding method (Kapur et al., 1985), and the maximum one among
533 the binarized component of 26-connected pixels was regarded as an apical junction network.
534 Then, we performed 3D skeletonization process for the images of apical junctions, and
535 obtained a graph network including nodes and edges of skeletonized voxels utilizing
536 distributed MATLAB codes with modifications (Kerschnitzki et al., 2013). Finally, to extract
537 the skeleton of apical cellular junctions (Fig. 3A), we screened out the skeletonized edges to
538 avoid over-skeletonization results in the following 3 criteria; (1) The edge length between

539 two nodes is less than 10 μm, (2) the edge length is shorter than two-fold linear length
540 between two nodes linked with the corresponding edge, (3) the number of edges from a node
541 is more than 3. The screening process under the criteria produced 96% left from the total
542 number of raw skeletonized edges. The relative angle of apical junction edges against the
543 longitudinal axis of epididymal tubule was calculated as $\vartheta_j = \left|\cos^{-1}\left(\hat{\mathbf{g}}_j \cdot \hat{\mathbf{l}}\right)\right|$ where j is an
544 index of apical edges, $\hat{\mathbf{g}}$ is an unit vector of apical edges, and $\hat{\mathbf{l}}$ is that of the longitudinal
545 axis of tubule, as shown in Figure 3B. For the signal quantification, we extracted signal
546 intensity of pMRLC or that of VANGL2 on the apical cellular junctions by using a thickened
547 skeleton of apical junctions with a dilation operator (3 × 3 × 3 voxels), and calculated
548 average values for each edge of thickened apical junction skeletons.
549
550 **(iii) Tubule Diameter in Inhibitor Assay**
551 First, we performed immunostaining for the E-cadherin of 8 different epididymides for each
552 inhibitor treatment to visualize the epididymal tubule as described above, and obtained the
553 volumetric images of 512 × 512 pixels using ×20 lens with z-axis interval of 5 μm. We
554 utilized the built-in module of a software platform, the Leica Suite X, (Leica), to create a
555 montage image of whole epididymis. Then, we manually extracted epididymal tubules from
556 maximum intensity projection images by erasing the efferent ductules and noise pixels due to
557 non-specific staining. From the preprocessed images, we obtained the centerline of
558 epididymal tubule by applying the built-in skeletonization algorithm in MATLAB for the
559 binary images obtained with arbitrarily determined thresholds, and finally calculated the
560 diameter along the centerline of tubule.
561
562 **(iv) pMRLC Signal Intensity along Epididymal Tubule**
563 First, we performed immunostaining for the pMRLC of 12 different epididymides as

564 described above with a minor modification: the dilution ratio of anti-pMRLC was 1:100.
565 Second, we obtained the volumetric images of 512 × 512 as described above using ×20 lens
566 with z-axis interval of 1 μm; we manually made montage images to avoid an overlap region
567 of composite images. Third, we manually erased signal intensity on pixels corresponding to
568 non-apical cellular region from the MIP images to obtain the centerline of epididymal tubule
569 as described above. Then, we calculated average values of pMRLC intensity within a circle
570 with a radius of 9 um along the epididymal tubule. Finally, we obtained the pMRLC signal
571 distribution along the epididymal tubule by smoothing the averaged signal intensity with a
572 moving average filter with a span of 40 μm – data in 20 μm range from the both ends of
573 tubule were omitted. The maximum value of vertical axis in Fig. 3H is 1 which corresponds
574 to the maximum intensity of 8 bit images. The horizontal axis of Fig. 3H was normalized by
575 the tubule length of each sample.
576
577 **(v) Correlation between the Number of Mitotic Cells and pMRLC Signal Intensity**
578 We used the data on the number of mitotic cells from our previous work (Hirashima and
579 Adachi, 2015) and one on the pMRLC intensity obtained in this study. We divided 30 bins
580 along the epididymal tubule and calculated maximum likelihood estimates with the Poisson
581 distribution for the number of mitotic cells and with the Gaussian distribution for the pMRLC
582 intensities in each bin. The Pearson's correlation coefficients are 0.49 (*P*-value=0.006) for
583 E15.5 and 0.56 (*P*-value=0.001) for E16.5.
584
585 **(vi) Apical Surface Area**
586 We obtained 1024 × 256 volumetric images of fluorescently-labeled F-actin in epididymal
587 tubules as described above using ×40 lens with z-axis interval of 1 μm, and randomly
588 collected samples of apical cell surface from image planes of 3 different epididymal

589 volumetric data on which the apical cell surfaces exhibited. Then, we calculated the apical
590 surface area by tracing the peripheral of apical cell surfaces manually.
591
592 **(vii) Cell Intercalation Rate for Tube Elongation (CITE)**
593 We first obtained time-lapsed volumetric images for epithelial dynamics from the head
594 region of 4 different samples at E15.5 through the live imaging as described above, and
595 collected time series data for a group of cells around mitotic cells. In particular, we sampled
596 those cells on an image plane perpendicular to the optical axis from the image data, and
597 focused on cross sections in-between the apical and basal part of cells. We defined
598 cytokinesis as an origin of time for our analysis, and analyzed data on cell intercalation
599 dynamics with time interval of 10 min ($\Delta t = 10\,\mathrm{min}$).
600 Next, based on an earlier study, we calculated the cell intercalation strain rate tensor $\mathbf{L}_{\mathbf{I}}^{t}$
601 at time *t* as follows:
602 $$\mathbf{L}_{\mathbf{I}}^{t} = \mathbf{L}_{\mathbf{T}}^{t} - \mathbf{L}_{\mathbf{C}}^{t},$$
603 where $\mathbf{L}_{\mathbf{T}}^{t}$ is a local tissue velocity gradient tensor, and $\mathbf{L}_{\mathbf{C}}^{t}$ is a cell shape strain rate tensor
604 (Blanchard et al., 2009). Because our analysis was performed in planar, the tensors are 2 × 2
605 matrices. For the calculation of a local tissue velocity gradient tensor $\mathbf{L}_{\mathbf{T}}^{t}$, we specified one
606 or two neighboring cells of a daughter cell from a mitotic cell that located an extension of the
607 division axis as central cells, and marked the adjacent cells of the central cells including the
608 central cells and the daughter cell as domain cells. Then, we manually traced each one of n
609 domain cells to obtain cell areas, cell shapes with the best fit ellipses, and cell centroids $\mathbf{r}_j^t$,
610 where j is an index of domain cells (see marked cells by yellow lines in Fig. S4A). Using
611 data of the cell centroids $\mathbf{r}_j^t$ and that of velocities $\mathbf{u}_j^t$, the local velocity gradient tensor was
612 obtained by the least squares approximations according to the following equation,

$$\mathbf{u}_j^t \approx \left\langle \mathbf{u}^t \right\rangle + \mathbf{L}_{\mathrm{T}} \left(\mathbf{r}_j^t - \left\langle \mathbf{r}^t \right\rangle \right),$$

where $\left\langle \mathbf{r}^t \right\rangle = \sum_j \mathbf{r}_j^t / n$, $\mathbf{u}_j^t = \left(\mathbf{r}_j^{t+\Delta t} - \mathbf{r}_j^t \right) / \Delta t$ and $\left\langle \mathbf{u}^t \right\rangle = \left(\left\langle \mathbf{r}^{t+\Delta t} \right\rangle - \left\langle \mathbf{r}^t \right\rangle \right) / \Delta t$. $\langle \cdot \rangle$ indicates an average within the domain.

For the calculation of the cell shape strain rate tensor $\mathbf{L}_{\mathbf{C}}^t$, we used lengths of principal axes of a fitted ellipse and angle of the major axis from the longitudinal axis of epididymal tubule to obtain a matrix $\mathbf{C}_j^t$ that represents the cell ellipse. Then, we calculated $\mathbf{L}_{\mathbf{C},j}^t$ from $\mathbf{C}_j^t$ and $\mathbf{C}_j^{t+\Delta t}$, and $\mathbf{L}_{\mathbf{C}}^t$ was calculated by taking the area-weighted average of $\mathbf{L}_{\mathbf{C},j}^t$ within the domain cells. Note that we normalized $\mathbf{L}_{\mathbf{C}}^t$ to satisfy that a trace of $\mathbf{L}_{\mathbf{C}}^t$ was equal to that of $\mathbf{L}_{\mathbf{T}}^t$, realizing that the cell intercalation strain rate tensor $\mathbf{L}_{\mathbf{I}}^t$ had zero dilation.

Finally, we obtained the CITE at time t (L_{ll}^t) from an element of the cell intercalation strain rate tensor:

$$\mathbf{L}_{\mathbf{I}}^t = \begin{pmatrix} L_{ll}^t & L_{lc}^t \\ L_{cl}^t & L_{cc}^t \end{pmatrix}.$$

Note that the $L_{ll}^t = -L_{cc}^t$.

The data were classified into two groups depending on the relative angle of cell division axis to the longitudinal axis of epididymal tubule – we defined the relative division angle of 0-30 degrees as longitudinal division and that of 60-90 degrees as circumferential division.

(III) Mathematical Modeling

(i) Basic Formalization of the Vertex Dynamics Model

We employed a vertex dynamics model (VDM), a type of cell-oriented model, to represent multi-cellular dynamics in epithelial tissues (Farhadifar et al., 2007; Fletcher et al., 2014; Nagai and Honda, 2001; Rauzi et al., 2008). In this model, a cell is geometrically regarded as

635 a polygon/polyhedron, of which vertices are elementary points that constitute the cell shape,
636 and a group of cells can be represented by a set of polygons/polyhedrons shared by
637 neighboring cells (Fletcher et al., 2013; Honda and Eguchi, 1980; Honda et al., 2004; Nagai
638 and Honda, 2001; Okuda et al., 2013). In this study, we paid notice to apical junctions of the
639 epididymal tubule on which a marker of tension generator pMRLC is only localized (Fig. 2A),
640 and modeled the developing single-layered epithelial tube as a flexible multicellular
641 membrane in 3D space according to earlier studies (Du et al., 2014; Osterfield et al., 2013).

642 In the VDM, the dynamics of position of vertex *i*, $\mathbf{r}_i$, obey the equation of motion based
643 on the principle of least potential energy *U* as follows:

644

645 $$\eta\left(\frac{d\mathbf{r}_i}{dt}-\langle\mathbf{v}_i\rangle\right)=-\nabla_i U\,, \qquad \text{Eq. (i-1)}$$

646 where η is a viscosity coefficient, and $\langle\mathbf{v}_i\rangle$ is a local velocity of vertex *i*, defined as

647 $$\langle\mathbf{v}_i\rangle=\frac{\sum_{\alpha_i}^{n_{\alpha_i}} d\mathbf{r}_{\alpha_i}/dt}{n_{\alpha_i}}\,, \qquad \text{Eq. (i-2)}$$

648 where α_i is an index for cells contacting to vertex *i*, n_{α_i} is a number of the cells
649 contacting to vertex *i*, and $\mathbf{r}_{\alpha_i}$ is a centroid of cell α_i (Mao et al., 2013; Okuda et al., 2014).
650 For a potential energy as a minimum expression to represent epididymal tubule cells, we
651 defined as

652

653 $$U=\sum_{\alpha}\left\{\frac{\lambda_{\mathrm{A}}}{2}\left(A_\alpha-A_\alpha^{\mathrm{O}}\right)^2+\frac{\lambda_{\mathrm{P}}}{2}P_\alpha^2\right\}+\sum_i\frac{\lambda_{\mathrm{B}}}{2}\kappa_i^2A_i+\sum_j\left\{\gamma_j^{\mathrm{cst}}L_j-\gamma_j^{\mathrm{ext}}H(L^{\mathrm{O}}-L_j)\right\}, \qquad \text{Eq. (i-3)}$$

654

655 according to earlier studies (Collinet et al., 2015; Farhadifar et al., 2007; Rauzi et al., 2008).
656 α, *i*, and *j* each denote an index of cells, that of vertices, and that of junctions/edges. The

657 first term represents the cell elasticity; λ_{A} is its coefficient, A_α is area of cell α, and A_α^{O}

658 is a target area of cells. The second term represents isotropic actomyosin contractility at the

659 periphery of apical junctions; λ_{P} is its coefficient and P_α is perimeter of the cell α. The

660 third term represents bending energy of the flexible epithelial membrane embedded in 3D

661 space; λ_{B} is its coefficient, κ_i is a discrete mean curvature defined at vertex *i* of triangular

662 meshes (Meyer et al., 2003), and A_i is summation of an area of triangular mesh fractions

663 around vertex *i*, each explained one by one. For calculation of the discrete mean curvature at

664 a vertex, let surface of the modeled epithelial membrane be a set of triangular meshes

665 consisting of both the vertex of cells and the centroid of cells (Fig. S1A). Then, we defined

666 the discrete mean curvature at vertex *i* as

667 $$\kappa_i = \frac{1}{2S_i}\left|\sum_{k\in V_i}\left(\cot\theta_{i,k}^1 + \cot\theta_{i,k}^2\right)\left(\mathbf{r}_i - \mathbf{r}_k\right)\right|, \qquad \text{Eq. (i-4)}$$

668 where *k* is an index of the triangular elements included in the set of 1-ring neighbor vertices

669 of the vertex *i*, V_i, S_i is total area of triangular meshes in V_i, $\theta_{i,k}^1$ and $\theta_{i,k}^2$ are each angle

670 depicted in Figure S1A'. See (Meyer et al., 2003) for more details. For calculation of A_i, let

671 us consider triangles consisting a vertex and its 1-ring neighbor cell centroids illustrated in

672 Figure S1A", and then sum the all triangles up around the vertex. In earlier studies, bending

673 energy was defined as a summation of inner product of unit normal vectors to the surfaces

674 between the adjacent cells (Du et al., 2014; Osterfield et al., 2013). This is valid when all

675 mesh size is ideally equal (Kantor and Nelson, 1987; Seung and Nelson, 1988); therefore, we

676 introduced the bending energy function based on the discrete curvature. The last term

677 represents anisotropic junction constriction/extension; $\gamma_j^{\mathrm{cst/ext}}$ is its coefficient assigned to

678 each edge, L_j is length of edge, L^{O} is a target edge length, and *H* is the Heaviside step

679 function. For the simulation in Fig. 1F-F", 4, and S1, $\gamma_j^{\mathrm{cst/ext}}$=0. The details of this term are

described later.

(ii) Normalized form of the model

By introducing a characteristic cell size A_0, the equations were transformed into nondimensionalized form to reduce the number of parameters as

$$\frac{d\mathbf{r}_i'}{dt'} - \left\langle \mathbf{v}_i' \right\rangle = -\nabla_i' U', \qquad \text{Eq. (ii-1)}$$

where $t' = t\lambda_{\mathrm{A}} A_0/\eta$, $\mathbf{r}_i' = \mathbf{r}_i/\sqrt{A_0}$, $\mathbf{r}_{\alpha_i}' = \mathbf{r}_{\alpha_i}/\sqrt{A_0}$, $\nabla' = \nabla\sqrt{A_0}$, $U' = U/\left(\lambda_{\mathrm{A}} A_0^2\right)$, and

$$U' = \sum_\alpha \left\{ \frac{1}{2}\left(A_\alpha' - A_\alpha'^{\mathrm{O}}\right)^2 + \frac{\lambda_{\mathrm{P}}'}{2} P_\alpha'^2 \right\} + \sum_i \frac{\lambda_{\mathrm{B}}'}{2} \kappa_i'^2 A_i' + \sum_j \left\{ \gamma_j'^{\mathrm{cst}} L_j' - \gamma_j'^{\mathrm{ext}} H(L^{\mathrm{O}} - L_j') \right\},$$

Eq. (ii-2)

where $A_\alpha' = A_\alpha/A_0$, $A_\alpha'^{\mathrm{O}} = A_\alpha^{\mathrm{O}}/A_0$, $P_\alpha' = P_\alpha/\sqrt{A_0}$, $\kappa_i' = \kappa_i\sqrt{A_0}$, $A_i' = A_i/A_0$, $L_j' = L_j/\sqrt{A_0}$, $L^{\mathrm{O}} = L^{\mathrm{O}}/\sqrt{A_0}$, $\lambda_{\mathrm{P}}' = \lambda_{\mathrm{P}}/\left(\lambda_{\mathrm{A}} A_0\right)$, $\lambda_{\mathrm{B}}' = \lambda_{\mathrm{B}}/\left(\lambda_{\mathrm{A}} A_0^2\right)$, $\gamma_j'^{\mathrm{cst/ext}} = \gamma_j^{\mathrm{cst/ext}}/\left(\lambda_{\mathrm{A}} A_0^{-3/2}\right)$. In addition, we introduced a normalized simulation time defined as $\tau' = t'/T^{\mathrm{cycle}}$, where T^{cycle} is an average cell cycle length, which will be explained. We used these variables and equations, Eq. (ii-1) and (ii-2), for the numerical simulations in this study.

(iii) Cell intercalation, Proliferation, and Simulation Conditions

As for the cell intercalation, we assumed that edge rearrangement occurred when the normalized length of edge became smaller than 0.05 and the edge length was set to be 0.1 after the edge rearrangement. See (Fletcher et al., 2013) for details of the edge rearrangement.

As for the cell proliferation, we introduced the average cell cycle length T^{cycle}, and set

702 cell cycle length of each cell T_α^{cycle} obey the normal distribution of which the mean is T^{cycle}

703 and the standard deviation is 5% of the mean, i.e., $T_\alpha^{\text{cycle}} \sim N(T^{\text{cycle}}, 0.05T^{\text{cycle}})$. Also, we

704 introduced normalized cell cycle time of each cell as $\tau_\alpha'^{\text{cycle}} = t_\alpha'^{\text{cycle}} / T_\alpha^{\text{cycle}}$, where $t_\alpha'^{\text{cycle}}$ is

705 nondimensionalized cell cycle time of cell α. $\tau_\alpha'^{\text{cycle}}$ at t'=0 was assigned within 0 to 0.95

706 in uniform distribution. As the average cell cycle length in the epididymal tubule can be

707 roughly estimated as 24 hours and cell volume tends to get increasing within the apical

708 surface of epididymal tubule since 50-100 min before the cytokinesis, we simply modeled the

709 cell dynamics during cell cycle as $A_\alpha'^{\text{target}} = 1$ for $0 \le \tau_\alpha'^{\text{cycle}} < 0.95$, $A_\alpha'^{\text{target}} = 20\tau_\alpha'^{\text{cycle}} - 18$ for

710 $0.95 \le \tau_\alpha'^{\text{cycle}} < 1$, and the cell divides with returning $A_\alpha'^{\text{target}}$ of daughter cells to 1.The type of

711 cell division orientation was set as follows – circumferential/longitudinal division: uniform

712 distribution in a range of $\pm 0.05\pi$ from the circumferential/longitudinal axis of tube, and

713 non-biased division: uniform distribution in all range of θ defined in the local coordinate at

714 cell (Fig. 1C).

715 As initial condition for the simulation, we set that a virtual tube was composed of 14

716 cells along the circumferential direction based on our observation and of 30 cells along the

717 longitudinal axis as for extensive numerical simulations. The cross-sectional center of the

718 tube was set at *y*=0 and *z*=0 of global coordinate and the tube was put along the *x* axis. As

719 boundary condition, the following energy was added to the original potential energy U' at

720 tip cells of the tube:

721

722 $$\sum_{\alpha_{\text{tip}}} \lambda'_{\text{bnd}} \left(\sqrt{(r'^{y}_{\alpha_{\text{tip}}})^2 + (r'^{z}_{\alpha_{\text{tip}}})^2} - R'_0 \right)^2, \qquad \text{Eq. (iii-1)}$$

723

724 where α_{tip} is an index for the tip cells of tube, λ'_{bnd} is its coefficient, R'_0 is a normalized

725 mean radius of the tube to a characteristic cell length $\sqrt{A_0}$ in the initial setting, $r'^{y}_{\alpha_{\mathrm{tip}}}$, and

726 $r'^{z}_{\alpha_{\mathrm{tip}}}$ each represent the relative position of center of cells α_{tip} on *y* and *z* axis to $\sqrt{A_0}$. This

727 energy restricts displacement of the cells α_{tip} in radial direction of the tube, which imitates

728 physical constraints by the vas deferens and the efferent ducts as boundary tissues of the

729 epididymal tubule. We set $\lambda'_{\mathrm{bnd}} = 0.1$ in the simulations. The results do not vary qualitatively

730 even without the boundary energy term Eq. (iii-1).

731

732 **(iv) Mechano-responsive and Scheduled regimes**

733 In the following, we explain the last two terms of Eq. (ii-2): the anisotropic edge constriction

734 and extension after the cell intercalation. We here introduce a state variable assigned to each

735 cell, $\Theta_\alpha = \{0,1,2\}$; $\Theta_\alpha = 0,1,2$ represent a naïve state (colored in white, Fig. 6B),

736 edge-constriction state (red, Fig. 6B), and edge-extension state (blue, Fig. 6B), respectively.

737 For all cells, $\Theta_\alpha = 0$, γ'^{cst}_j=0, and γ'^{ext}_j=0, unless otherwise noted. In our simulation, the

738 following procedures were conducted for both 'mechano-responsive' and 'scheduled' regime.

739 First, cells α' that might become a constricting cell were selected and let the state variable

740 of the cell $\Theta_{\alpha'} = 1$; the way of selecting cells depends on each regime, i.e, the

741 mechano-responsive or the scheduled regime. Second, one of the edges that orients to

742 circumferential axis of the tube (the angle ϑ_j is within 70° – 90°) was selected among all

743 edges composing the cells α', and index the edge j'. Then, state of cells including the

744 edge j' turned to $\Theta_{\alpha'} = 1$. Third, the constriction of edge j' was performed according to a

745 schedule as shown in Figure S4A; we set the edge kept constricting in a period τ'^{cst} via

746 transition period τ'^{trns} from the starting point of edge constriction by an assumption with

747 phosphorylation process of pMRLC. The maximum value of $\gamma'^{\mathrm{cst}}_{j'}$ was set to be γ'^{cst}. $\Theta_{\alpha'}$

and $\gamma'^{\mathrm{cst}}_{j'}$ return to 0 at the end of edge constriction process. In this study, parameter dependence of τ'^{cst} and that of γ'^{cst} were examined and determined (Fig. S4B), and we set $\tau'^{\mathrm{trns}} = 0.02$. Finally, if the edge arrangement occurred during the process of edge constriction ($\Theta_{\alpha'} = 1$), then the state of cells having the rearranged edge changes to $\Theta_{\alpha'} = 2$ and the edge becomes an extension mode, in which the rearranged edge converges to a constant target length; $\gamma'^{\mathrm{cst}}_{j'} = 0$, $\gamma'^{\mathrm{ext}}_{j'} = 0.01$, and $L^{\mathrm{O}} = 0.1$. We set the period of edge extension as $\tau'^{\mathrm{ext}} = 0.02$. $\Theta_{\alpha'}$ and $\gamma'^{\mathrm{ext}}_{j'}$ return to 0 after the process of edge extension. Our implementation for the edge extension process is based on an earlier report that the junction after the cell intercalation grows due to local polarized force driven by medial actomyosin contraction (Collinet et al., 2015).

As for the way of selecting the cells α' in the first step described above, we adopted the two: mechano-responsive and scheduled regime. On the mechano-responsive regime, we supposed that the epididymal tubule cells could receive mechanical stress provided by adjacent cells, and a stress tensor in cells α in the local cell coordinate system *O'* was defined as

$$\sigma_\alpha = \left(A'_\alpha - A'^{\mathrm{O}}_\alpha\right)\mathbf{I} + \sum_{j_\alpha}\left(\lambda'_{\mathrm{P}} + \gamma'^{\mathrm{cst}}_{j_\alpha} - \gamma'^{\mathrm{ext}}_{j_\alpha}\right)\frac{\mathbf{a}_{j_\alpha} \otimes \mathbf{a}_{j_\alpha}}{L'_{j_\alpha} A'_\alpha}, \qquad \text{Eq. (iv-1)}$$

where $\mathbf{I}$ is a unit tensor, j_α is an index of edges composing the cell α, $\mathbf{a}$ is a vector representing the relative position of two vertices composing the edge j_α (Batchelor, 1970; Ishihara and Sugimura, 2012; Sugimura and Ishihara, 2013). Denoting a diagonal element of the tensor σ_α corresponding to the longitudinal axis of the tube and that to the circumferential axis as $\sigma^{\mathrm{long}}_\alpha$ and $\sigma^{\mathrm{circ}}_\alpha$, we then defined the cell tension anisotropy as

$$\rho_\alpha = \sigma_\alpha^{\text{long}} - \sigma_\alpha^{\text{circ}}. \qquad \text{Eq. (iv-2)}$$

Note that the cell tension anisotropy ρ_α is a time-dependent variable. In the mechano-responsive regime, the cells were assigned as α' when ρ_α was over a threshold ρ^*, of which parameter dependency for the resulting tube morphology was examined (Fig. S4B).

On the scheduled regime, the cells α' were randomly selected but timing of the selection was predetermined according to the schedule shown in Figure 6C; Figure 6C shows the fraction of cells having constricting edges to all tube cells in the mechano-responsive regime (*n*=10, gray), and its mean (black). In our simulation, we used the following logistic function (blue) by fitting the mean curve with the least-squared method:

$$f(\tau') = k_1\left(1+\exp\left[-k_2(\tau'-k_3)\right]\right)^{-1} \qquad \text{Eq. (iv-3)}$$

with $k_1 = 0.1$, $k_2 = 0.01$, and $k_3 = 0.17$.

(v) Morphological and Mechanical Quantities in Simulation

We used the following morphological quantities in the simulation; 1) tube length, i.e., longitudinal linear length between distal edges of tube, 2) tube diameter, i.e., mean diameter of circumferentially-averaged diameter through the centerline of tube, and 3) curvedness, i.e., averaged curvature of the vertices throughout the tube defined as $\sum_i \kappa_i' A_i' \Big/ \sum_i A_i'$.

For the cell tension anisotropy ρ_α, refer to the Eq. (iv-2). For the tube tension anisotropy in Figure 1F, the stress tensor in the tube was defined as

$$\sigma_{\text{tube}} = \left[\sum_{\alpha} \left(A'_{\alpha} - A'^{\text{O}}_{\alpha} \right) A'_{\alpha} \mathbf{I} + \sum_{j} \left(\lambda'_{\text{P}} + \gamma'^{\text{cst}}_{j} - \gamma'^{\text{ext}}_{j} \right) \frac{\mathbf{a}_j \otimes \mathbf{a}_j}{L'_j} \right] \Big/ \sum_{\alpha} A'_{\alpha} , \qquad \text{Eq. (v-1)}$$

according to earlier studies (Batchelor, 1970; Ishihara and Sugimura, 2012), and using its diagonal element $\sigma^{\text{long}}_{\text{tube}}$ and $\sigma^{\text{circ}}_{\text{tube}}$, we introduced

$$\rho_{\text{tube}} = \sigma^{\text{long}}_{\text{tube}} - \sigma^{\text{circ}}_{\text{tube}} \qquad \text{Eq. (v-2)}$$

as the tube tension anisotropy. $\sigma^{\text{long}}_{\text{tube}}$ and $\sigma^{\text{circ}}_{\text{tube}}$ each correspond to the tube longitudinal tension and the tube circumferential tension appeared in Figure S1.

(vi) Determination of Parameter Values (Fig. S1 and Fig. S4)

Parameter values used in this study were (i) $\lambda'_{\text{P}}=10^{-2}$, $\lambda'_{\text{B}}=10^{0.75}$, (ii) $T^{\text{cycle}}=10^{3.75}$, (iii) $\rho^* = 0.1$, $\gamma'^{\text{cst}} = 1$, and $\tau'^{\text{cst}} = 0.167$ unless otherwise noted. As for (i), we determined the values, at which there were less variations at $t'=1000$ from the initial configuration (Fig. S1B and S1B'). Note that no proliferation was implemented for this analysis. As for (ii), we examined the parameter dependence of cell proliferation rate $1/T^{\text{cycle}}$ to the morphological and the mechanical quantities at $\tau' = 1$ (Fig. S1C). The results show that the cell division orientation less affected to the tube shape (length and diameter) in faster cell proliferation rate. In addition, smooth surface of tube was not maintained if the cell proliferation rate was larger than $10^{-3.5}$ (see curvedness in Fig. S1C). This is because the cell proliferation rate is faster than relaxation time of tube in the dynamics. We determined as $T^{\text{cycle}}=10^{3.75}$. As for (iii), we examined the parameter dependence of ρ^*, γ'^{cst}, and τ'^{cst} to the tube shape and its variance at $\tau' = 1$ (Fig. S4B). We first determined $\rho^* = 0.1$ because the coefficient of

817 variation (CV) became larger at $\rho^* = 0.08$ and there were less differences of the mean
818 values to the variation of γ'^{cst} at $\rho^* = 0.125$. Then, we determined $\gamma'^{\mathrm{cst}} = 1$ because this
819 point is at a boundary for both the mean and the CV. Finally, as for τ'^{cst}, we arbitrarily set
820 the value because there were less differences in any values.
821

822 ## (IV) Others

823 **(i) Statistical Hypothesis Testing**

824 Exact information of the statistical tests, sample sizes, test statistics, and *P*-values were
825 described in the Supplemental Information. Statistical hypothesis testing was performed
826 according to (Zar, 2014). *P*-values of less than 0.05 were considered to be statistically
827 significant in two-tailed tests, and were classified as 4 categories; * ($P<0.05$), ** ($P<0.01$),
828 *** ($P<0.001$), and n.s. (not significant, i.e., $P \geq 0.05$).
829

830 **(ii) Replicates and Sample Number**

831 All replicates in this study are biological replicates. The *n* in the figure legends indicates the
832 number of samples used for each analysis as described below.
833 Figure 1D and E: *n* indicates the number of cells sampled from 6 epididymides collected
834 from a pregnant mouse.
835 Figure 2D-F′: *n* indicates the number of apical edges sampled from 8 epididymides collected
836 from 2 pregnant mice.
837 Figure 2G′: *n* indicates the number of measured points sampled from 8 epididymides
838 collected from 3 pregnant mice.
839 Figure 3B and B′: *n* indicates the number of epididymides collected from 3 pregnant mice.
840 Figure 3D′ and D′′: *n* indicates the number of cells randomly chosen from 3 epididymides
841 collected from a pregnant mouse.

Figure 5E: *n* indicates the number of a group of cells sampled from 4 epididymides each collected from 4 pregnant mice.

Figure 7D-D′′: *n* indicates the number of cells randomly chosen from 10 epididymides collected from 3 pregnant mice.

Figure 7E′ and E′′: *n* indicates the number of pregnant mice.

(iii) Graph

Except for boxplot, we used mean as representative values, and error bars represent standard deviation. Boxplots were drawn using R (GNU project).

(iv) Software

For digital image processing, we used MATLAB (MathWorks) and Image J (National Institute of Health). For graphics, we used MATLAB (MathWorks), R (GNU project), Gnuplot (Free Software), and Paraview (Kitware). For statistical analysis, we used MATLAB (MathWorks) and R (GNU project).

Additional files

Additional files include full information of statistical hypothesis testing, and supplementary five figures.

Author Contributions

T.H. performed experiments and simulations, and analyzed all data; T.H. and T.A. wrote the manuscript.

Acknowledgements

This work was supported by the Platform Project for Supporting in Drug Discovery and Life Science Research (Platform for Dynamic Approaches to Living System) from the MEXT and the AMED, and by the JSPS KAKENHI grant 15K18541. We would like to thank T. Furukawa of Osaka Univ. for kindly providing the Pax2-Cre mice.

Competing Interests

The authors declare that no competing interests exist.

875 # References

876 **Abe, T., Kiyonari, H., Shioi, G., Inoue, K. I., Nakao, K., Aizawa, S. and Fujimori, T.**
877 (2011). Establishment of conditional reporter mouse lines at ROSA26 locus for live cell
878 imaging. *Genesis* **49**, 579–590.

879 **Andrew, D. J. and Ewald, A. J.** (2010). Morphogenesis of epithelial tubes: Insights into
880 tube formation, elongation, and elaboration. *Dev Biol* **341**, 34–55.

881 **Batchelor, G. K.** (1970). The stress system in a suspension of force-free particles. *J . Fluid*
882 *Mech* **41**, 545–570.

883 **Beloussov, L. V** (2015). *Morphomechanics of Development*. Springer.

884 **Bertet, C., Sulak, L. and Lecuit, T.** (2004). Myosin-dependent junction remodelling
885 controls planar cell intercalation and axis elongation. *Nature* **429**, 667–671.

886 **Blanchard, G. B., Kabla, A. J., Schultz, N. L., Butler, L. C., Sanson, B., Gorfinkiel, N.,**
887 **Mahadevan, L. and Adams, R. J.** (2009). Tissue tectonics: morphogenetic strain rates,
888 cell shape change and intercalation. *Nat. Methods* **6**, 458–464.

889 **Bosveld, F., Bonnet, I., Guirao, B., Tlili, S., Wang, Z., Petitalot, A., Marchand, R.,**
890 **Bardet, P.-L., Marcq, P., Graner, F., et al.** (2012). Mechanical Control of
891 Morphogenesis by Fat/Dachsous/Four-Jointed Planar Cell Polarity Pathway. *Science*
892 *(80-.).* **336**, 724–727.

893 **Collinet, C., Rauzi, M., Lenne, P. and Lecuit, T.** (2015). Local and tissue-scale forces drive
894 oriented junction growth during tissue extension. *Nat. Cell Biol.* **17**, 1247–1258.

895 **Dong, B., Hannezo, E. and Hayashi, S.** (2014). Balance between Apical Membrane Growth
896 and Luminal Matrix Resistance Determines Epithelial Tubule Shape. *Cell Rep*.

897 **Du, X., Osterfield, M. and Shvartsman, S. Y.** (2014). Computational analysis of
898 three-dimensional epithelial morphogenesis using vertex models. *Phys. Biol.* **11**, 66007.

899 **Eisenhoffer, G. T., Loftus, P. D., Yoshigi, M., Otsuna, H., Chien, C.-B., Morcos, P. A.**

900 **and Rosenblatt, J.** (2012). Crowding induces live cell extrusion to maintain
901 homeostatic cell numbers in epithelia. *Nature* **484**, 546–549.
902 **Farhadifar, R., Röper, J.-C., Aigouy, B., Eaton, S. and Jülicher, F.** (2007). The influence
903 of cell mechanics, cell-cell interactions, and proliferation on epithelial packing. *Curr.*
904 *Biol.* **17**, 2095–104.
905 **Fischer, E., Legue, E., Doyen, A., Nato, F., Nicolas, J.-F., Torres, V., Yaniv, M. and**
906 **Pontoglio, M.** (2006). Defective planar cell polarity in polycystic kidney disease. *Nat.*
907 *Genet.* **38**, 21–23.
908 **Fletcher, A. G., Osborne, J. M., Maini, P. K. and Gavaghan, D. J.** (2013). Implementing
909 vertex dynamics models of cell populations in biology within a consistent computational
910 framework. *Prog. Biophys. Mol. Biol.* **113**, 299–326.
911 **Fletcher, A. G., Osterfield, M., Baker, R. E. and Shvartsman, S. Y.** (2014). Vertex
912 models of epithelial morphogenesis. *Biophys. J.* **106**, 2291–2304.
913 **Galkin, V. E., Orlova, A. and Egelman, E. H.** (2012). Actin filaments as tension sensors.
914 *Curr. Biol.* **22**,.
915 **Gudipaty, S. A., Lindblom, J., Loftus, P. D., Redd, M. J., Edes, K., Davey, C. F.,**
916 **Krishnegowda, V. and Rosenblatt, J.** (2017). Mechanical stretch triggers rapid
917 epithelial cell division through Piezo1. *Nature* **543**, 118–121.
918 **Guillot, C. and Lecuit, T.** (2013). Mechanics of epithelial tissue homeostasis and
919 morphogenesis. *Science* **340**, 1185–9.
920 **Hayakawa, K., Tatsumi, H. and Sokabe, M.** (2011). Actin filaments function as a tension
921 sensor by tension-dependent binding of cofilin to the filament. *J. Cell Biol.* **195**, 721–
922 727.
923 **Hirashima, T.** (2014). Pattern Formation of an Epithelial Tubule by Mechanical Instability
924 during Epididymal Development. *Cell Rep.* **9**, 866–73.

Hirashima, T. (2016). Mathematical study on robust tissue pattern formation in growing epididymal tubule. *J. Theor. Biol.* **407**, 71–80.

Hirashima, T. and Adachi, T. (2015). Procedures for the Quantification of Whole-Tissue Immunofluorescence Images Obtained at Single-Cell Resolution during Murine Tubular Organ Development. *PLoS One* **10**, e0135343.

Honda, H. and Eguchi, G. (1980). How much does the cell boundary contract in a monolayered cell sheet? *J. Theor. Biol.* **84**, 575–588.

Honda, H., Tanemura, M. and Nagai, T. (2004). A three-dimensional vertex dynamics cell model of space-filling polyhedra simulating cell behavior in a cell aggregate. *J. Theor. Biol.* **226**, 439–453.

Honda, H., Nagai, T. and Tanemura, M. (2008). Two different mechanisms of planar cell intercalation leading to tissue elongation. *Dev. Dyn.* **237**, 1826–36.

Hufnagel, L., Teleman, A. A., Rouault, H., Cohen, S. M. and Shraiman, B. I. (2007). On the mechanism of wing size determination in fly development. *Proc. Natl. Acad. Sci. U. S. A.* **104**, 3835–40.

Ishihara, S. and Sugimura, K. (2012). Bayesian inference of force dynamics during morphogenesis. *J. Theor. Biol.* **313**, 201–211.

Joseph, A., Yao, H. and Hinton, B. T. (2009). Development and morphogenesis of the Wolffian/epididymal duct, more twists and turns. *Dev Biol* **325**, 6–14.

Kantor, Y. and Nelson, D. R. (1987). Crumpling transition in polymerized membranes. *Phys. Rev. Lett.* **58**, 2774–2777.

Kapur, J. N., Sahoo, P. K. and Wong, A. K. C. (1985). A new method for gray-level picture thresholding using the entropy of the histogram. *Comput. Vision, Graph. Image Process.* **29**, 140.

Karner, C. M., Chirumamilla, R., Aoki, S., Igarashi, P., Wallingford, J. B. and Carroll,

950 **T. J.** (2009). Wnt9b signaling regulates planar cell polarity and kidney tubule
951 morphogenesis. *Nat. Genet.* **41**, 793–799.
952 **Kerschnitzki, M., Kollmannsberger, P., Burghammer, M., Duda, G. N., Weinkamer, R.,**
953 **Wagermaier, W. and Fratzl, P.** (2013). Architecture of the osteocyte network
954 correlates with bone material quality. *J. Bone Miner. Res.* **28**, 1837–1845.
955 **Kovács, M., Tóth, J., Hetényi, C., Málnási-Csizmadia, A. and Seller, J. R.** (2004).
956 Mechanism of blebbistatin inhibition of myosin II. *J. Biol. Chem.* **279**, 35557–35563.
957 **Kunimoto, K., Bayly, R. D., Vladar, E. K., Vonderfecht, T., Gallagher, A.-R. and**
958 **Axelrod, J. D.** (2017). Disruption of Core Planar Cell Polarity Signaling Regulates
959 Renal Tubule Morphogenesis but Is Not Cystogenic. *Curr. Biol.*
960 **Mammoto, T., Mammoto, A. and Ingber, D. E.** (2013). Mechanobiology and
961 Developmental Control. *Annu. Rev. Cell Dev. Biol.* **29**, 27–61.
962 **Mao, Y., Tournier, A. L., Hoppe, A., Kester, L., Thompson, B. J. and Tapon, N.** (2013).
963 Differential proliferation rates generate patterns of mechanical tension that orient tissue
964 growth. *EMBO J.* **32**, 2790–2803.
965 **Meyer, M., Desbrun, M., Schr, P. and Barr, A. H.** (2003). Discrete Differential-Geometry
966 Operators for Triangulated 2-Manifolds. *Vis. Math. III* 113–134.
967 **Morin, X. and Bellaïche, Y.** (2011). Mitotic Spindle Orientation in Asymmetric and
968 Symmetric Cell Divisions during Animal Development. *Dev. Cell* **21**, 102–119.
969 **Nagai, T. and Honda, H.** (2001). A dynamic cell model for the formation of epithelial
970 tissues. *Philos. Mag. Part B* **81**, 699–719.
971 **Nishimura, T., Honda, H. and Takeichi, M.** (2012). Planar cell polarity links axes of
972 spatial dynamics in neural-tube closure. *Cell* **149**, 1084–1097.
973 **Ohyama, T. and Groves, A. K.** (2004). Generation of Pax2-Cre Mice by Modification of a
974 Pax2 Bacterial Artificial Chromosome. *Genesis* **38**, 195–199.

975 **Okuda, S., Inoue, Y., Eiraku, M., Sasai, Y. and Adachi, T.** (2013). Reversible network
976 reconnection model for simulating large deformation in dynamic tissue morphogenesis.
977 *Biomech. Model. Mechanobiol.* **12**, 627–644.
978 **Okuda, S., Inoue, Y., Eiraku, M., Adachi, T. and Sasai, Y.** (2014). Vertex dynamics
979 simulations of viscosity-dependent deformation during tissue morphogenesis. *Biomech.*
980 *Model. Mechanobiol.* **14**, 413–425.
981 **Osterfield, M., Du, X., Schüpbach, T., Wieschaus, E. and Shvartsman, S. Y.** (2013).
982 Three-Dimensional Epithelial Morphogenesis in the Developing Drosophila Egg. *Dev.*
983 *Cell* **24**, 400–410.
984 **Rauzi, M., Verant, P., Lecuit, T. and Lenne, P.-F.** (2008). Nature and anisotropy of
985 cortical forces orienting Drosophila tissue morphogenesis. *Nat. Cell Biol.* **10**, 1401–10.
986 **Sasai, Y.** (2013). Cytosystems dynamics in self-organization of tissue architecture. *Nature*
987 **493**, 318–26.
988 **Savin, T., Kurpios, N. A., Shyer, A. E., Florescu, P., Liang, H., Mahadevan, L. and**
989 **Tabin, C. J.** (2011). On the growth and form of the gut. *Nature* **476**, 57–62.
990 **Seung, H. S. and Nelson, D. R.** (1988). Defects in flexible membranes with crystalline order.
991 *Phys. Rev. A* **38**, 1005–1018.
992 **Shraiman, B. I.** (2005). Mechanical feedback as a possible regulator of tissue growth. *Proc.*
993 *Natl. Acad. Sci. U. S. A.* **102**, 3318–3323.
994 **Stewart, M. P., Helenius, J., Toyoda, Y., Ramanathan, S. P., Muller, D. J. and Hyman,**
995 **A. a** (2011). Hydrostatic pressure and the actomyosin cortex drive mitotic cell rounding.
996 *Nature* **469**, 226–230.
997 **Sugimura, K. and Ishihara, S.** (2013). The mechanical anisotropy in a tissue promotes
998 ordering in hexagonal cell packing. *Development* **140**, 4091–4101.
999 **Susaki, E. A., Tainaka, K., Perrin, D., Kishino, F., Tawara, T., Watanabe, T. M.,**

1000 **Yokoyama, C., Onoe, H., Eguchi, M., Yamaguchi, S., et al.** (2014). Whole-brain
1001 imaging with single-cell resolution using chemical cocktails and computational analysis.
1002 *Cell* **157**, 726–739.
1003 **Tang, N., Marshall, W. F., McMahon, M., Metzger, R. J. and Martin, G. R.** (2011).
1004 Control of Mitotic Spindle Angle by the RAS-Regulated ERK1/2 Pathway Determines
1005 Lung Tube Shape. *Science (80-.).* **333**, 342–345.
1006 **Thompson, D. W.** (1942). *On growth and form.*
1007 **Tomaszewski, J., Joseph, A., Archambeault, D. and Yao, H. H.** (2007). Essential roles of
1008 inhibin beta A in mouse epididymal coiling. *Proc Natl Acad Sci U S A* **104**, 11322–
1009 11327.
1010 **Walck-Shannon, E. and Hardin, J.** (2014). Cell intercalation from top to bottom. *Nat. Rev.*
1011 *Mol. Cell Biol.* **15**, 34–48.
1012 **Watanabe, T., Hosoya, H. and Yonemura, S.** (2007). Regulation of Myosin II Dynamics
1013 by Phosphorylation and Dephosphorylation of Its Light Chain in Epithelial Cells. *Mol.*
1014 *Biol. Cell* **18**, 605–616.
1015 **Xu, B., Washington, A. M., Domeniconi, R. F., Ferreira Souza, A. C., Lu, X., Sutherland,**
1016 **A. and Hinton, B. T.** (2016). Protein tyrosine kinase 7 is essential for tubular
1017 morphogenesis of the Wolffian duct. *Dev. Biol.* **412**, 219–233.
1018 **Yokomizo, T., Yamada-Inagawa, T., Yzaguirre, A. D., Chen, M. J., Speck, N. A. and**
1019 **Dzierzak, E.** (2012). Whole-mount three-dimensional imaging of internally localized
1020 immunostained cells within mouse embryos. *Nat. Protoc.* **7**, 421–431.
1021 **Zallen, J. A. and Blankenship, J. T.** (2008). Multicellular dynamics during epithelial
1022 elongation. *Semin. Cell Dev. Biol.* **19**, 263–270.
1023 **Zar, J. H.** (2014). *Biostatistical Analysis, 5th Edition*.
1024
1025

Figure Legends

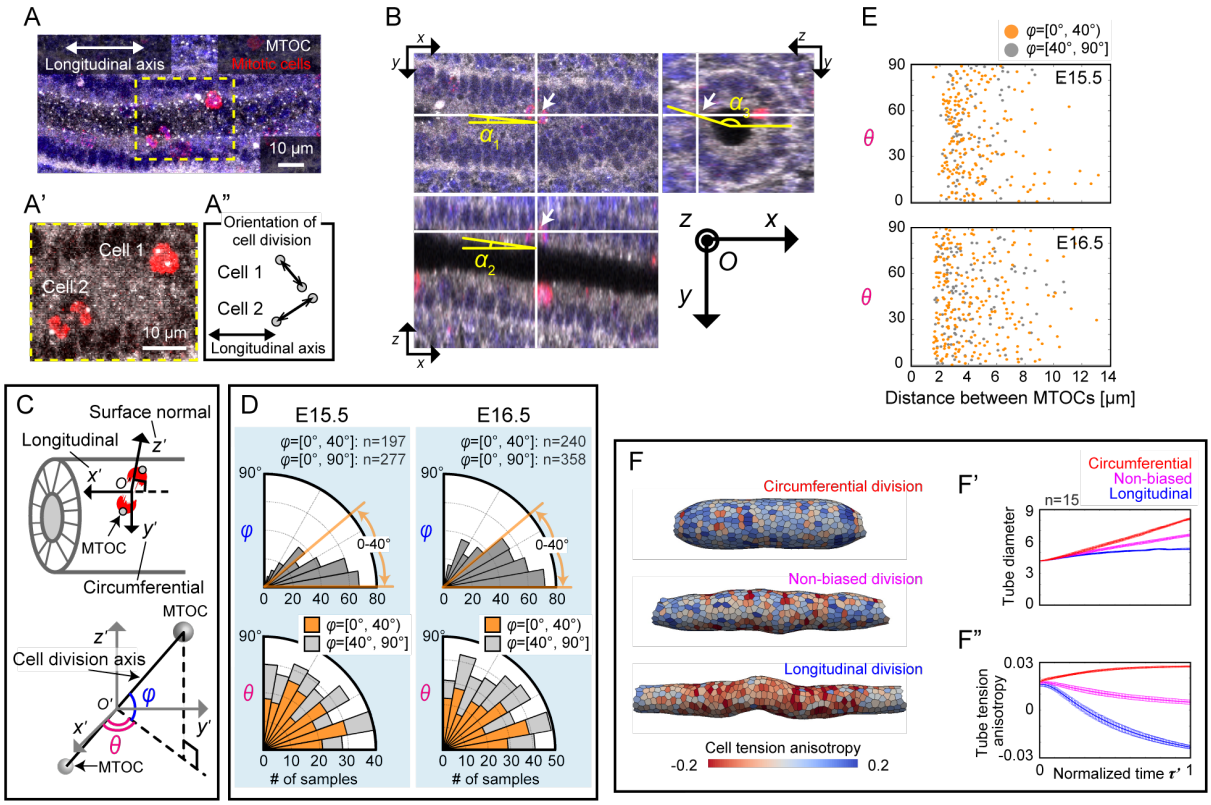

Figure 1 Cell division orientation determines the mechanical stress and tubule morphology.

(A) Maximum intensity projection (MIP) of immunostained images for the pHH3 (mitotic cells, red) and γ-tubulin (MTOCs, white). (A′ and A′′) Magnified view of the dotted square in (A), displaying the two cells divide in different orientations. Scale bars: 10 μm. (B) Measurement of cell division orientation in the tubule. Arrows indicate the center position of the mitotic cell. Using the three angles α_1, α_2, and α_3, the observation coordinate O is transformed into the local coordinate O' in Fig. 1C. (C) Illustration of the local coordinates. (D) The angle distributions of the cell division orientation. Colors in the θ distribution represent samples, of which φ ranges from 0-40 degrees (orange) and from 40-90 degrees (gray). (E) Scatter plot for the distance between MTOCs and the angle θ. The sample number is the same as in (D). (F-F′′) Model simulations in different cell division orientations.

1040 (F) The vertex dynamics model simulation of proliferating tubes. The color represents the
1041 cell tension anisotropy. (F′ and F′′) Time course of morphological and mechanical quantities
1042 along the normalized simulation time τ'. See the Materials and Methods (III-iv) and (III-v)
1043 for those quantities and Materials and Methods (III-ii) for the definition of τ'. n=15.
1044

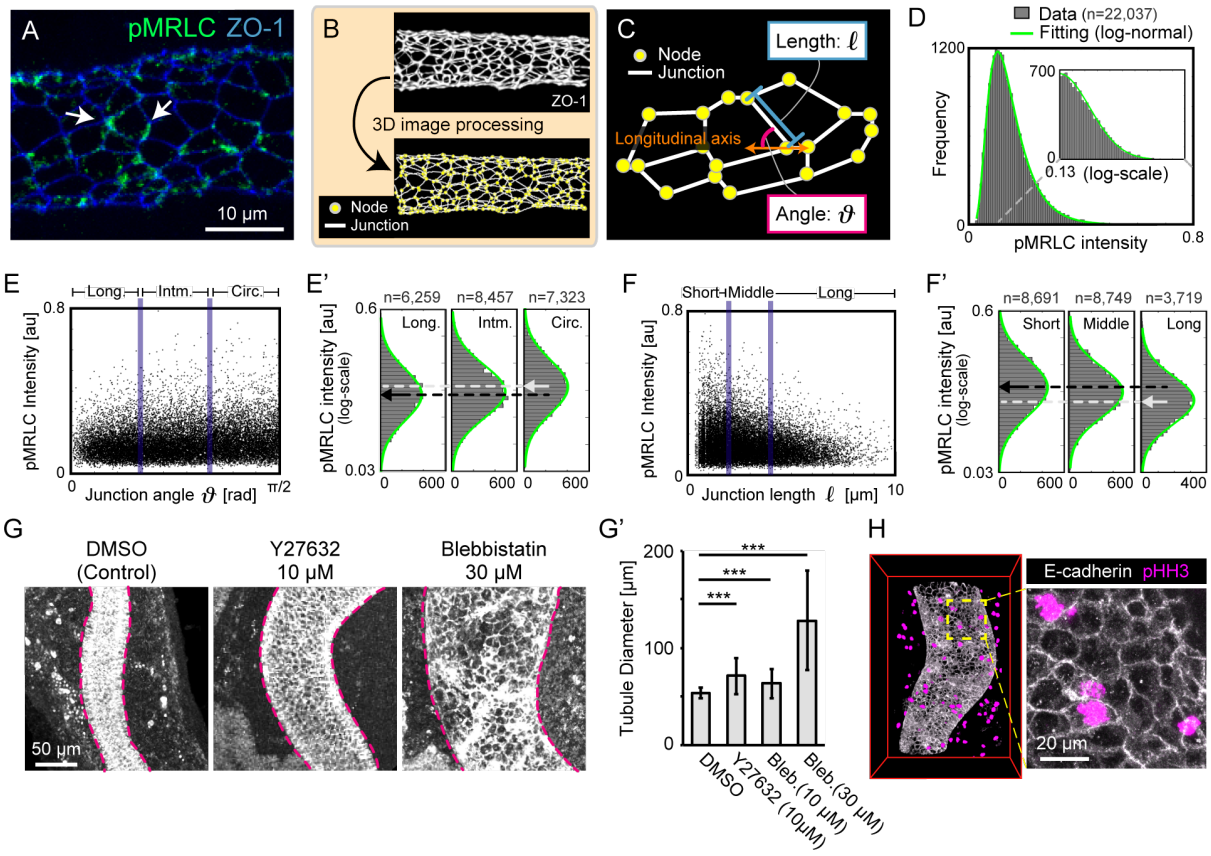

Figure 2 Polarized apical junction constriction is required for the maintenance of tubule radial size.

(A) MIP of co-immunostained images of pMRLC (green) and ZO-1 (blue). Arrows indicate pMRLC localization at circumferential apical junctions. Scale bar: 10 μm. (B) Digital processing from immunofluorescence images for the ZO-1 detects nodes and junctions of apical surfaces. (C) Illustration of the junction length ℓ and junction angle ϑ that measures the angle from the longitudinal axis of tubules. (D) Histogram of pMRLC intensity (gray) fitted with a log-normal distribution (green). The small window displays the tail of distribution. n=22,037. (E-F′) Relationship between the pMRLC intensity and the junction angle/length. The log-scale histograms are shown in three divided groups. Black arrows represent the mean intensity in the longitudinal/short group and white arrows represent that in the circumferential/long group. (G and G′) Morphological change of tubules in the inhibitor treatment. (G) MIP of immunofluorescence images for the E-cadherin of head region of

1059 epididymis. Scale bar: 50 μm. Magenta dotted lines represent the basal line of tubules in the
1060 MIP images. (G′) The tubule diameter for the treatments. *n*=320. (H) 3D images of the
1061 co-immunostaining for E-cadherin (white) and pHH3 (magenta) in 30 μM Blebbistatin
1062 treatment. Scale bar: 20 μm.
1063
1064

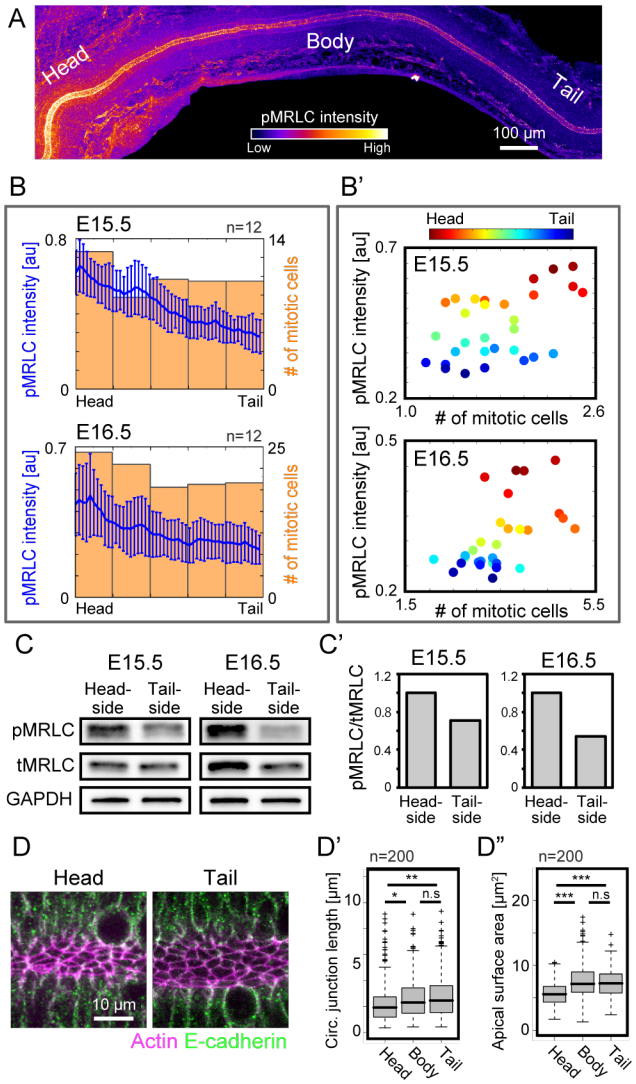

Figure 3 Apical junctional constriction and cell division shows positive correlation. (A) MIP of pMRLC immunostaining at the whole-tissue scale. Scale bar: 100 µm. (B) Spatial profile of pMRLC intensity (blue) and the number of mitotic cells (orange) along the tubule. *n*=12. (B′) The pMRLC intensity versus the mitotic cell number. The color indicates position of data in the tubule. (C and C′) Myosin activity quantification by immunoblotting. (D-D′′) Apical junction morphology visualized by staining for the F-actin and E-cadherin. *n*=200. Scale bar: 10 µm.

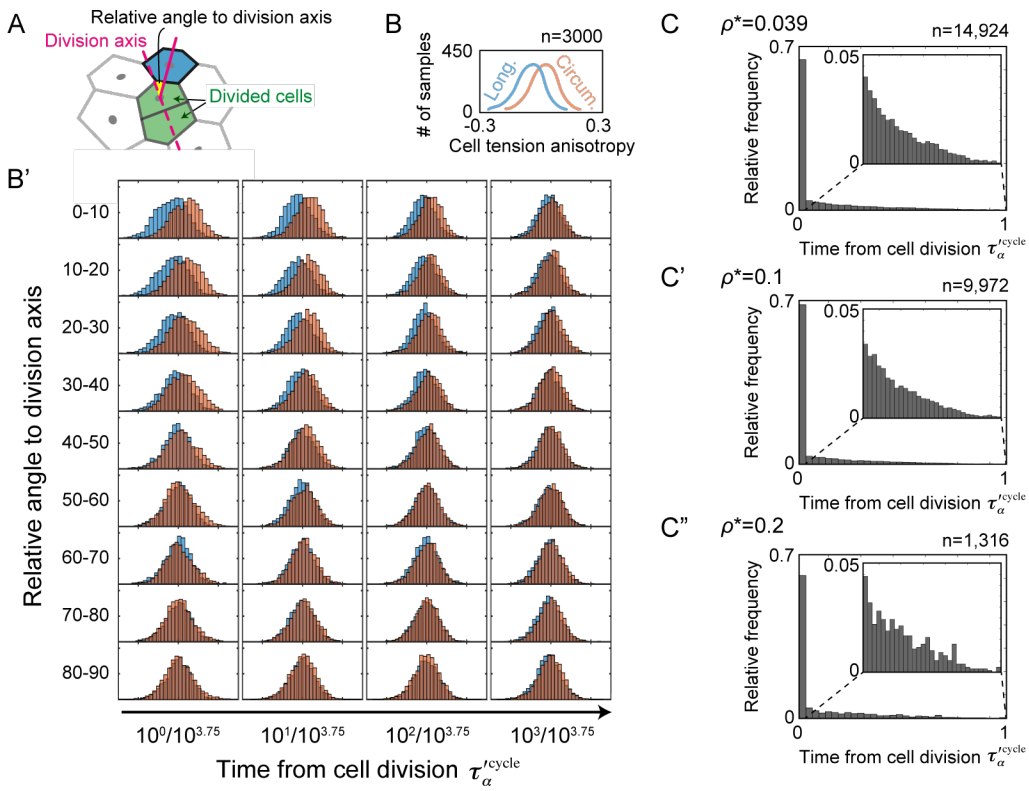

Figure 4 Computational analysis of cell stress influenced by cell division in tubes. (A) The schematics for glossary. The cell tension anisotropy was calculated in cells (e.g., colored in blue) neighboring to the divided cells (green). (B and B′) Histograms of cell tension anisotropy against the cell divisions. (B) The explanatory illustration for the histograms. Red indicates the case of circumferential cell division and blue indicates the case of longitudinal cell division. (B′) Histograms of the cell tension anisotropy in various cases of the relative angle to the cell division axis (vertical) and in those of the elapsed time of neighbors' cell division $\tau_\alpha'^{cycle}$ (horizontal). (C-C′′) Histograms of the elapsed time after the cell division $\tau_\alpha'^{cycle}$ when the cell tension anisotropy is over various thresholds (ρ^*=0.039, 0.1, and 0.2) in neighboring cells on the circumferential axis. The tail of histograms is magnified in the small windows.

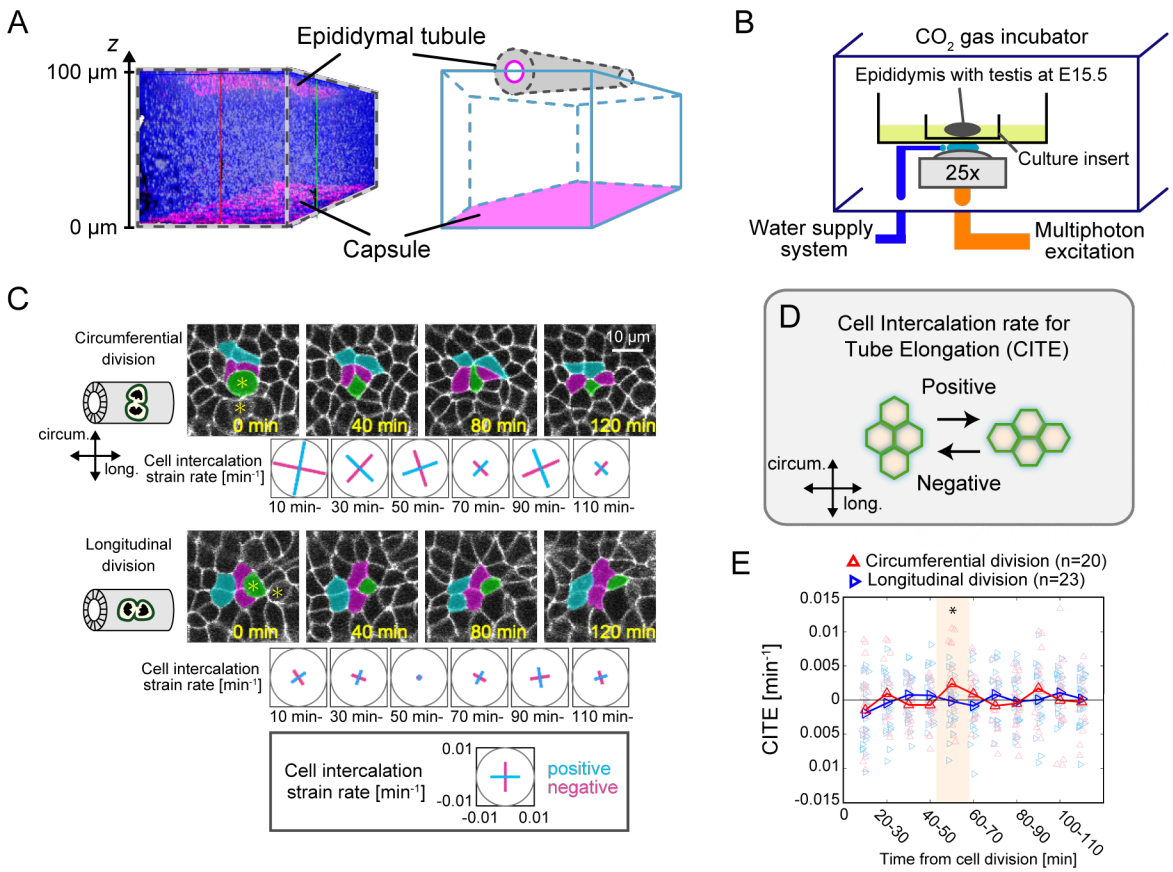

Figure 5 Live imaging revealed that the oriented cell division occurs following to the circumferential cell division.

(A) The dimensions of epididymis. The rendering image from the immunofluorescence for the ZO-1 (magenta) (left) and its schematics (right). (B) The schematics for the incubator-integrated multiphoton excitation microscopy system. (C) Snapshots from live imaging data in the case of the circumferential and longitudinal cell divisions. Time origin is at the timing of cytokinesis completion. Asterisks represent daughters of divided cell, one of which is colored artificially in green. Some cells are also colored for easy visualization. The scale and sign for cell intercalation strain rate is shown in the bottom. Scale bar: 10 µm. (D) Schematics for the CITE. (E) The time series data for the case of circumferential cell division (red, n=20) and that of the longitudinal division (blue, n=23). Time zone in which the mean value is not statistically zero is highlighted.

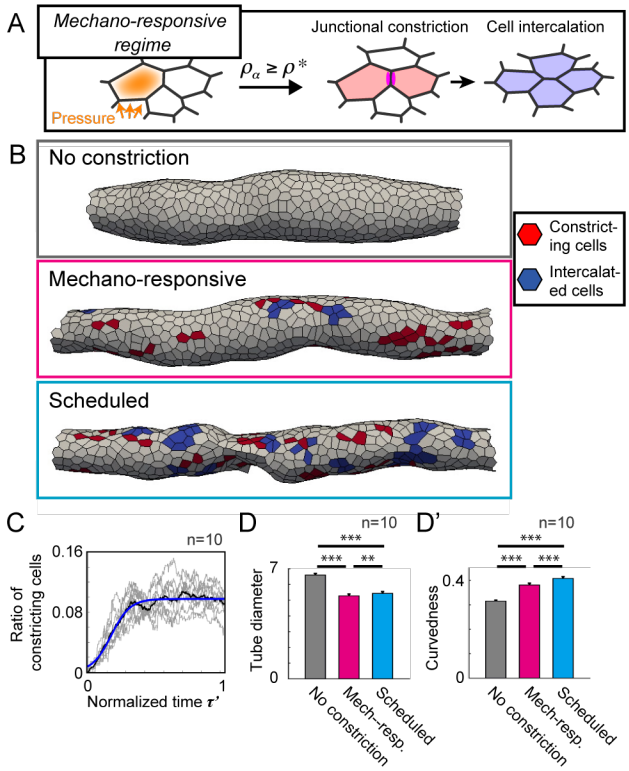

Figure 6 Model simulations suggest that the mechano-responsive cell behavior explains the maintenance of tubule radial size.

(A) Schematics for the mechano-responsive regime. In this regime, the circumferential junction constriction starts when the cell tension anisotropy becomes larger than the threshold ρ^* due to the pressure from circumferentially-neighboring cells. (B) Generated tubes in different regimes: no constriction, mechano-responsive, and scheduled. Red color in the tubes represents cells constricting the circumferential junction and blue represents cells that have completed the cell intercalation. (C) The ratio of constricting cells to the total cells over the normalized simulation time τ' in the mechano-responsive regime: data in each simulation (gray), the mean value (black) and fitting with the logistic function (blue). *n*=10. (D and D′) Resulting morphological quantities of tubes, the tube diameter and the tube curvedness, in different regimes. See the Materials and Methods (III-vi) for the definition of those morphological quantities. *n*=10.

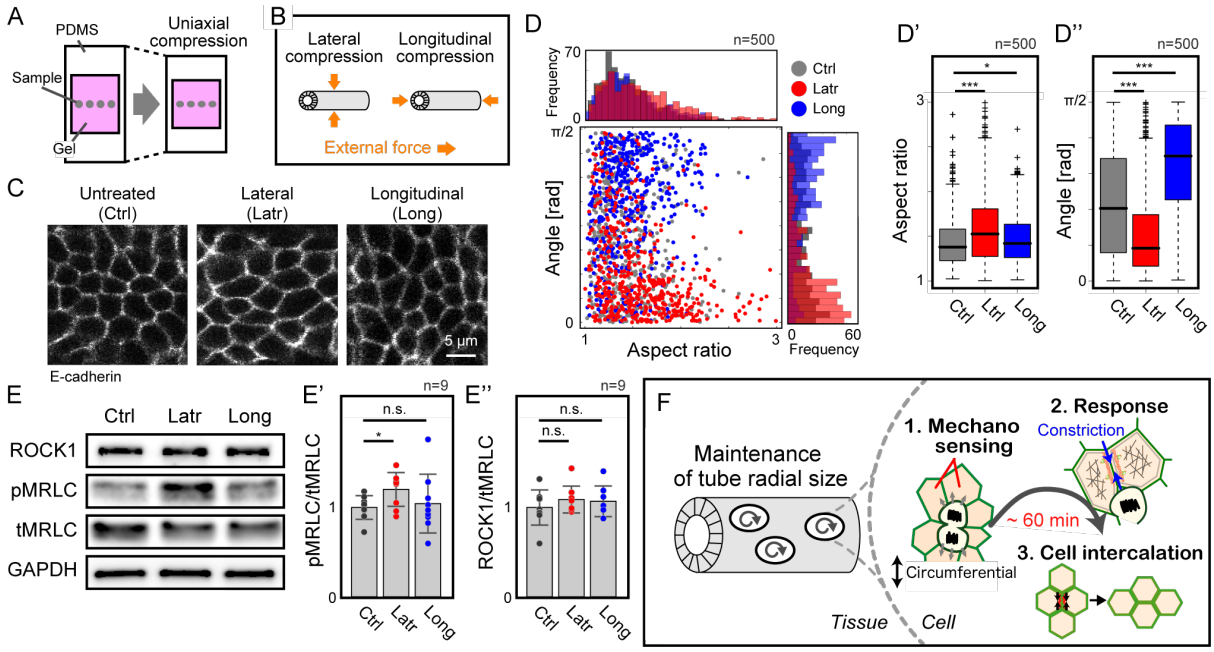

Figure 7 Mechanical perturbation assays uncovered that the myosin is activated anisotropically in the tubule axis.

(A and B) Schematics for the uniaxial compression assays. (C) Morphology of the tubule cells following the mechanical treatments. The cell shape was recognized by immunofluorescence for the E-cadherin. Scale bar: 5 μm. (D-D´´) The aspect ratio and the major axis angle for each treatment: control (gray), lateral compression (red), and longitudinal compression (blue). The data are shown as scatter plot and histogram in (D) and as boxplot in (D´ and D´´). *n*=500. (E-E´´) Immunoblotting and quantification of myosin activity and ROCK1 for the mechanical treatments. The tubule cells activate myosin as a cellular response to lateral compression. (E´ and E´´) The data are normalized to the mean value in the control. *n*=9. (F) Model for the maintenance of tubule radial size.

Additional files (Supplemental Information)

Anisotropic Cellular Mechanoresponse for Radial Size Maintenance of Developing Epithelial Tubes

Tsuyoshi Hirashima and Taiji Adachi

This file includes:

- Statistical Hypothesis Testing
- Supplementary Figures S1 to S5
- Still images and captions for Movies 1 to 3

Statistical Hypothesis Testing

The statistical tests, sample sizes, test statistics, and *P*-values were described below. *P*-values of less than 0.05 were considered to be statistically significant in two-tailed tests, and were classified as 4 categories; * ($P<0.05$), ** ($P<0.01$), *** ($P<0.001$), and n.s. (not significant, i.e., $P \geq 0.05$).

- Figure 1D, φ at E15.5

Note: The range of data was transformed to 0-360º for circular distributions.

H_0: The population of φ at E15.5 is uniformly distributed around the circle.

H_A: The population of φ at E15.5 is not uniformly distributed around the circle.

The Rayleigh test. n=277, Test statistic: Z=35.51, $P<0.001$; Reject H_0.

- Figure 1D, θ at E15.5

Note: The range of data was transformed to 0-360º for circular distributions.

H_0: The population of θ at E15.5 is uniformly distributed around the circle.

H_A: The population of θ at E15.5 is not uniformly distributed around the circle.

The Rayleigh test. n=197 (0-40º), Test statistic: Z=0.40, P=0.67; Do not reject H_0.

The Rayleigh test. n=277 (0-90º), Test statistic: Z=0.25, P=0.78; Do not reject H_0.

- Figure 1D, φ at E16.5

Note: The range of data was transformed to 0-360º for circular distributions.

H_0: The population of φ at E16.5 is uniformly distributed around the circle.

H_A: The population of φ at E16.5 is not uniformly distributed around the circle.

The Rayleigh test. n=358, Test statistic: Z=27.32, $P<0.001$; Reject H_0.

➢ Figure 1D, θ at E16.5

Note: The range of data was transformed to 0-360º for circular distributions.

H_0: The population of θ at E16.5 is uniformly distributed around the circle.

H_A: The population of θ at E16.5 is not uniformly distributed around the circle.

The Rayleigh test. n=240 (0-40º), Test statistic: Z=1.95, P=0.14; Do not reject H_0.

The Rayleigh test. n=358 (0-90º), Test statistic: Z=0.57, P=0.56; Do not reject H_0.

➢ Figure 2E´

Note: The data were transformed on logarithmic scale.

H_0: The mean intensities of pMRLC among the three groups of junction angle are all equal.

H_A: The mean intensities of pMRLC among the three groups of junction angle are not all equal.

One-way analysis of variance. n=6,259 (Longitudinal), n=8,457 (Intermediate), n=7,323 (Circumferential), Test statistic: F=165.47, P<0.001; Reject H_0.

Multiple comparisons using the Tukey-Kramer Test with unequal sample sizes: P<0.001 (Long. vs. Intm.), P<0.001 (Long. vs. Circ.), and P<0.001 (Intm. vs. Circ.).

➢ Figure 2F´

Note: The data were transformed on logarithmic scale.

H_0: The mean intensities of pMRLC among the three groups of junction length are all equal.

H_A: The mean intensities of pMRLC among the three groups of junction length are not all equal.

One-way analysis of variance. n=8,691 (Short), n=8,749 (Middle), n=3,719 (Long), Test statistic: F=306.65, P<0.001; Reject H_0.

Multiple comparisons using the Tukey-Kramer test with unequal sample sizes: P<0.001

(Short. vs. Middle), $P<0.001$ (Short vs. Long), and $P<0.001$ (Middle vs. Long).

- Figure 3D′

H_0: The circumferential edge length is the same in all three regions of epididymal tubule.

H_A: The circumferential edge length is not the same in all three regions of epididymal tubule.

The Kruskal-Wallis test, n=200 for all groups, Test statistic: H=14.84, $P<0.001$; Reject H_0.

Steel-Dwass multiple comparisons: P=0.016 (Head vs. Body), P=0.001 (Head vs. Tail), P=0.61 (Body vs. Tail).

- Figure 3D′′

H_0: The apical surface area is the same in all three regions of epididymal tubule.

H_A: The apical surface area is not the same in all three regions of epididymal tubule.

The Kruskal-Wallis test, n=200 for all groups, Test statistic: H=89.58, $P<0.001$; Reject H_0.

Steel-Dwass multiple comparisons: $P<0.001$ (Head vs. Body), $P<0.001$ (Head vs. Tail), P=0.71 (Body vs. Tail).

- Figure 5C

H_0: The mean value of CITE in a certain time zone from the cell division is equal to zero.

H_A: The mean value of CITE in a certain time zone from the cell division is not equal to zero.

t test, n=20 in the case of circumferential cell division and n=23 in that of longitudinal one,

Test statistic: absolute value of t: $|t|$

[Circ., 10-20 min]: $|t|$=0.97, P=0.34; Do not reject H_0

[Circ., 20-30 min]: $|t|$=1.01, P=0.32; Do not reject H_0

[Circ., 30-40 min]: $|t|$=1.12, P=0.29; Do not reject H_0

[Circ., 40-50 min]: $|t|$=1.06, P=0.30; Do not reject H_0

[Circ., 50-60 min]: $|t|$=2.37, P=0.03; Reject H_0

[Circ., 60-70 min]: $|t|$=1.50, P=0.15; Do not reject H_0

[Circ., 70-80 min]: $|t|$=1.09, P=0.29; Do not reject H_0

[Circ., 80-90 min]: $|t|$=0.54, P=0.59; Do not reject H_0

[Circ., 90-100 min]: $|t|$=1.75, P=0.10; Do not reject H_0

[Circ., 100-110 min]: $|t|$=0.04, P=0.97; Do not reject H_0

[Circ., 110-120 min]: $|t|$=0.35, P=0.73; Do not reject H_0

[Long., 10-20 min]: $|t|$=2.02, P=0.06; Do not reject H_0

[Long., 20-30 min]: $|t|$=0.51, P=0.61; Do not reject H_0

[Long., 30-40 min]: $|t|$=1.05, P=0.30; Do not reject H_0

[Long., 40-50 min]: $|t|$=0.98, P=0.34; Do not reject H_0

[Long., 50-60 min]: $|t|$=0.21, P=0.83; Do not reject H_0

[Long., 60-70 min]: $|t|$=1.03, P=0.31; Do not reject H_0

[Long., 70-80 min]: $|t|$=1.08, P=0.29; Do not reject H_0

[Long., 80-90 min]: $|t|$=0.31, P=0.76; Do not reject H_0

[Long., 90-100 min]: $|t|$=0.03, P=0.97; Do not reject H_0

[Long., 100-110 min]: $|t|$=1.75, P=0.09; Do not reject H_0

[Long., 110-120 min]: $|t|$=0.24, P=0.81; Do not reject H_0

- Figure 6D

H_0: The mean values of tube diameter among the three groups of regime are all equal.

H_A: The mean values of tube diameter among the three groups of regime are not all equal.

One-way analysis of variance, n=10 for all groups, F=791.10, P<0.001; Reject H_0.

Tukey multiple comparisons: P<0.001 (No constriction vs. Mech-resp.), P<0.001 (No constriction vs. Scheduled), and P=0.002 (Mech-resp vs. Scheduled).

1249

1250 ➢ Figure 6D´

1251 H_0: The mean values of curvedness among the three groups of regime are all equal.

1252 H_A: The mean values of curvedness among the three groups of regime are not all equal.

1253 One-way analysis of variance, n=10 for all groups, F=575.25, P<0.001; Reject H_0.

1254 Tukey multiple comparisons: P<0.001 (No constriction vs. Mech-resp.), P<0.001 (No

1255 constriction vs. Scheduled), and P<0.001 (Mech-resp vs. Scheduled).

1256

1257 ➢ Figure 7D´

1258 H_0: The aspect ratio of cells is the same in all three treatments of compression assay.

1259 H_A: The aspect ratio of cells is not the same in all three treatments of compression assay.

1260 The Kruskal-Wallis test, n=500 for all groups, Test statistic: H=42.10, P<0.001; Reject H_0.

1261 Steel multiple comparisons: P<0.001 (Control vs. Lateral), P=0.043 (Control vs.

1262 Longitudinal).

1263

1264 ➢ Figure 7D´´

1265 H_0: The angle of cells is the same in all three treatments of compression assay.

1266 H_A: The angle of cells is not the same in all three treatments of compression assay.

1267 The Kruskal-Wallis test, n=500 for all groups, Test statistic: H=366.04, P<0.001; Reject H_0.

1268 Steel multiple comparisons: P<0.001 (Control vs. Lateral), P<0.001 (Control vs.

1269 Longitudinal).

1270

1271 ➢ Figure 7E´

1272 H_0: The ratio of pMRLC to tMRLC is the same in all three treatments of compression assay.

1273 H_A: The ratio of pMRLC to tMRLC is not the same in all three treatments of compression

1274 assay.

1275 The Friedman test, n=9 for all groups, Test statistic: Q=6, P=0.049; Reject H_0.

1276 Steel multiple comparisons: P=0.039 (Control vs. Lateral), P=1.82 (Control vs.

1277 Longitudinal).

1278

1279 ➢ Figure 7E´

1280 H_0: The ratio of ROCK1 to tMRLC is the same in all three treatments of compression assay.

1281 H_A: The ratio of ROCK1 to tMRLC is not the same in all three treatments of compression

1282 assay.

1283 The Friedman test, n=9 for all groups, Test statistic: Q=1.56, P=0.46; Do not reject H_0.

1284 Steel multiple comparisons: P=0.50 (Control vs. Lateral), P=0.60 (Control vs. Longitudinal).

1285

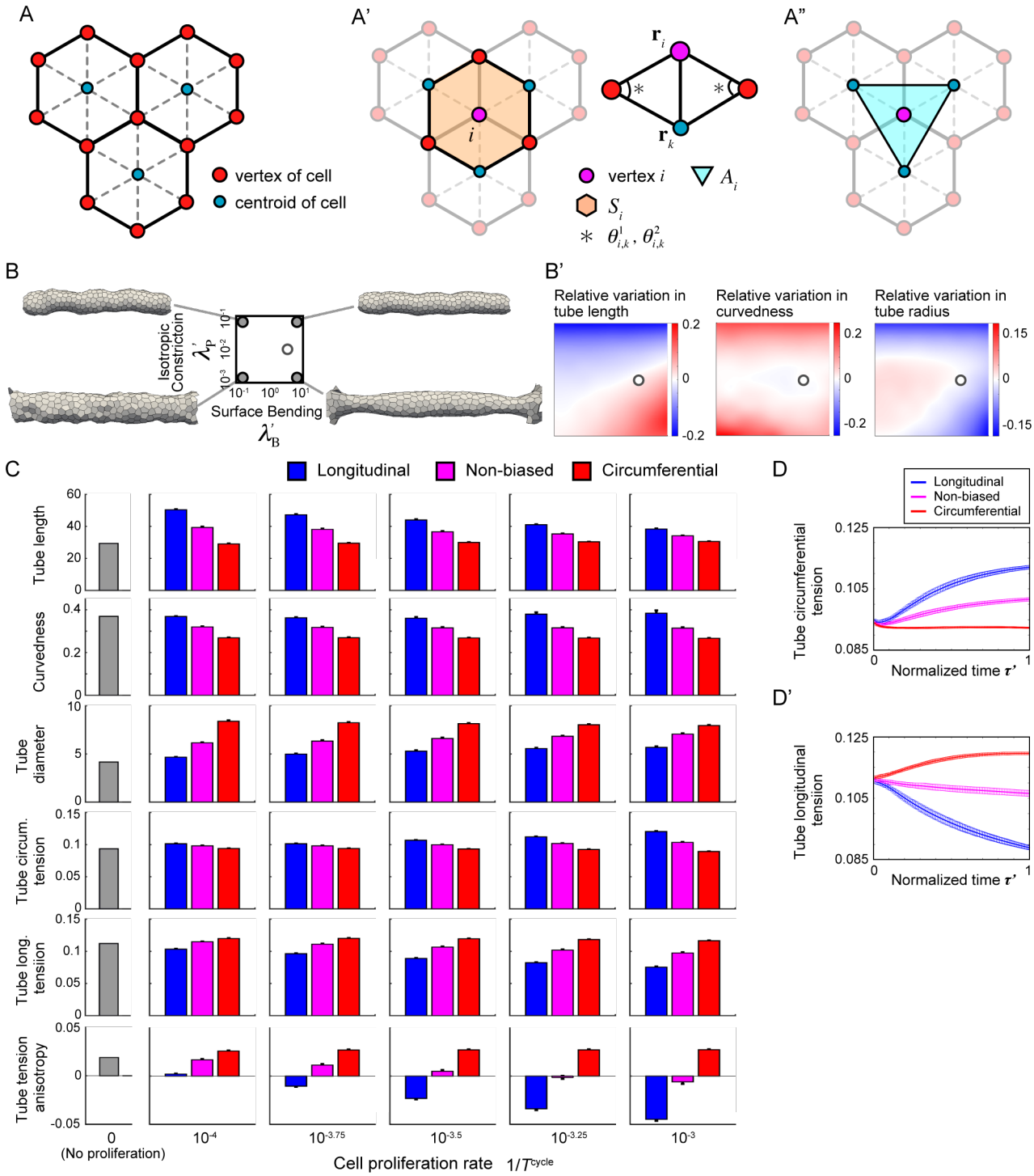

Figure S1 Preparation for the simulation without anisotropic junction constriction, corresponding to the Figure 2

(A-A") Schematics for the explanation of discrete curvature in the vertex model. See the Materials and Methods (III-ii) for the notations. (B and B') Diagram of generated tube morphology for parameters λ'_B and λ'_P, and relative variation of morphological quantities in

the absence of cell proliferation. Tubes are visualized in the four corners of parameter space (filled circles). Open circles represent parameter values used in this study. The axes labels are shown in B. (C) Parameter dependence of morphological and mechanical quantities for cell division orientation and cell proliferation rate. Color represents the type of cell division orientation. (D and D') Time course of tube circumferential tension and that of tube longitudinal tension. See the Materials and Methods (III-vi) for the definition of tube circumferential/longitudinal tension.

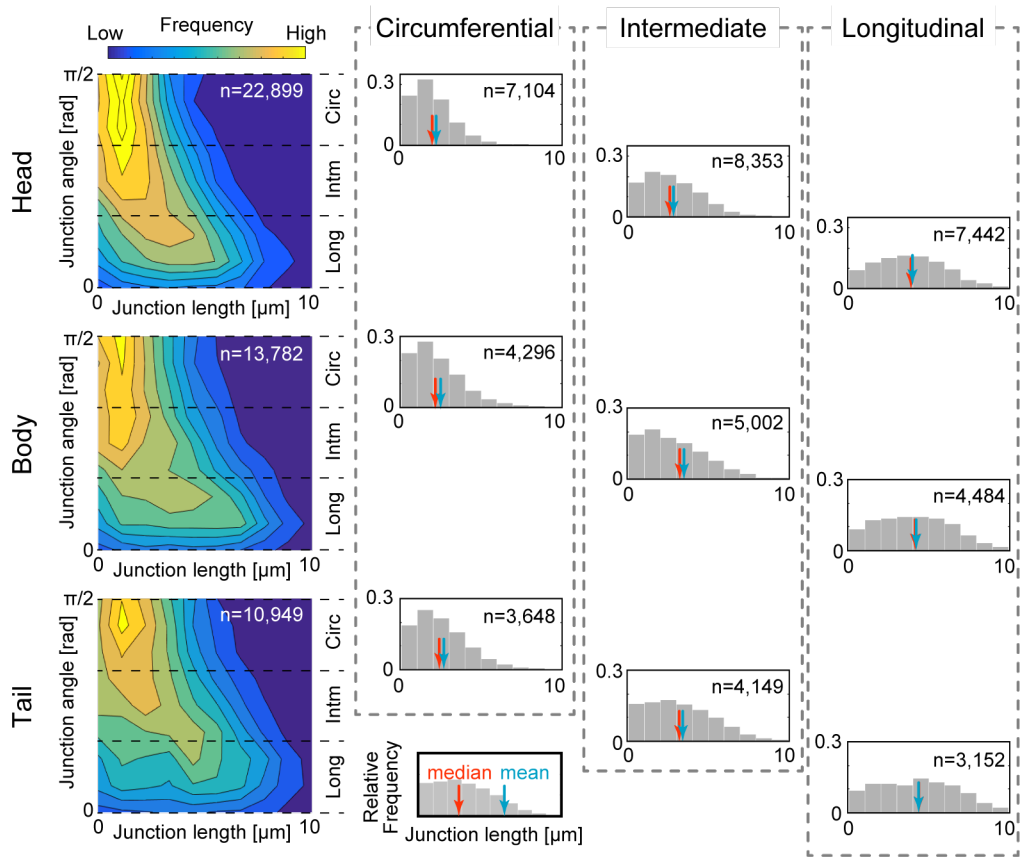

Figure S2 Apical junction length and angle, corresponding to the Figure 3

Frequency map on junction length ℓ and angle θ (left). Relative frequency in each region of epididymal tubule (Head, Body, and Tail) and angle category (Longitudinal, Intermediate, and Circumferential) is shown as histograms (right). The red/blue arrow indicates median/mean. The axis label of histograms is represented in the bottom. The circumferential junction length is shorter than the longitudinal junction length in any regions. In addition, the circumferential junction length in the head region is shorter than that in the tail region.

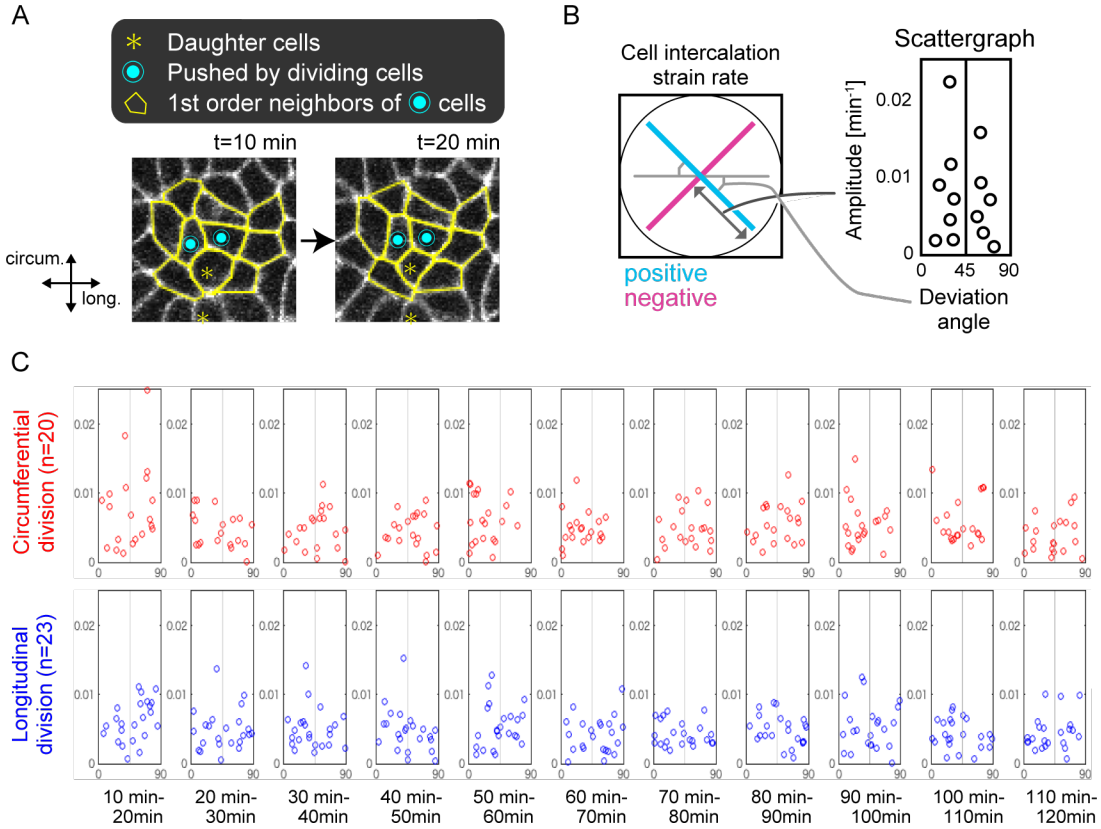

Figure S3 Measurement of cell intercalation strain rate from the live imaging data, corresponding to the Figure 5

(A) Illustration for target cells to calculate the cell intercalation strain rate. See the Materials and Methods (II-viii) for the details. (B) Graph representations for the cell intercalation strain rate. Orthogonal lines in the left graph represent principal strain rate. The amplitude and angle deviation of the positive principal strain rate (blue) in the left are expressed in the right angle-amplitude graph. (C) Time course of the cell intercalation strain rate as in the form of angle-amplitude graph for each type of cell division orientation: circumferential cell division and longitudinal one.

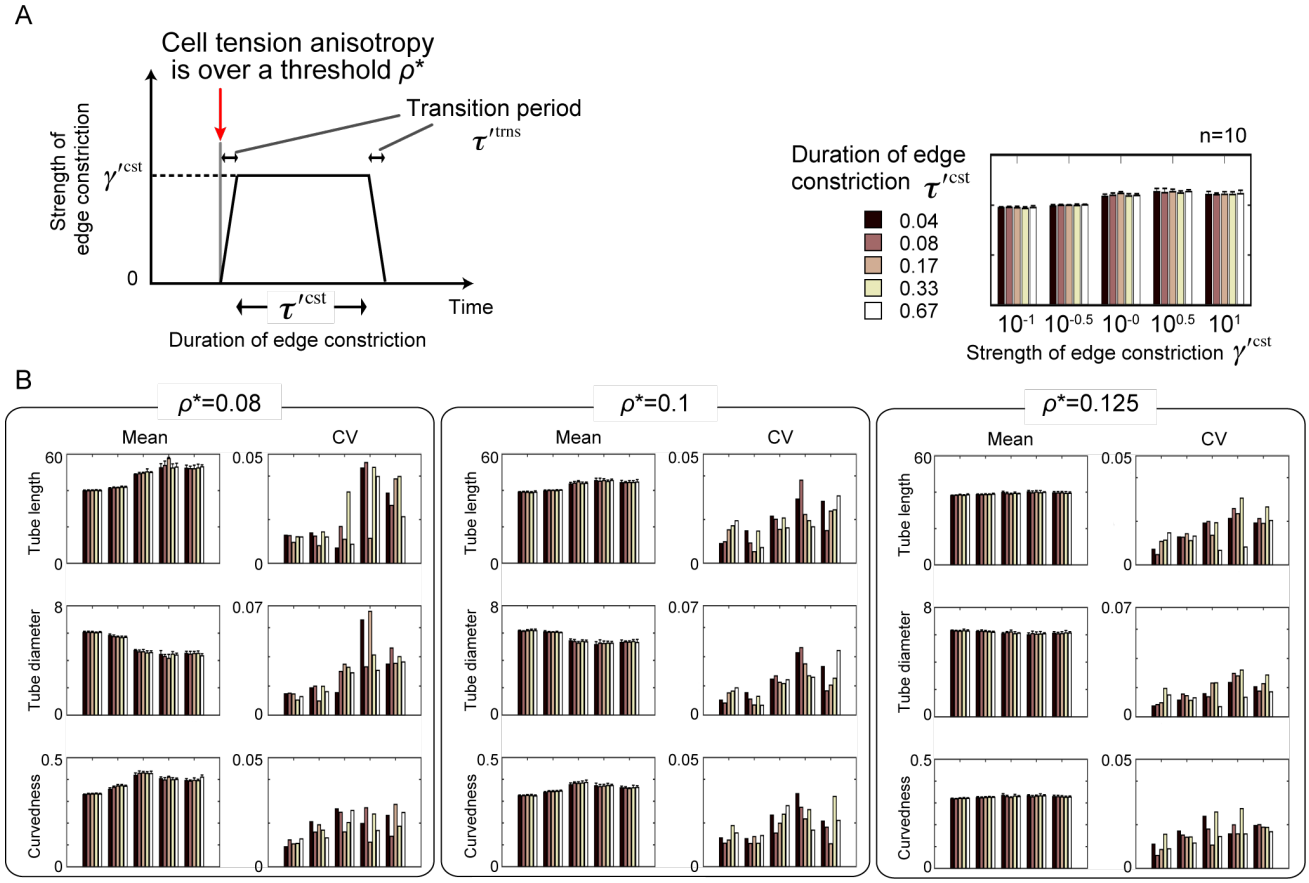

Figure S4 Preparation for the simulations in the mechano-responsive regime, corresponding to the Figure 6

(A) Schematics for the model. See the Materials and Methods (III-v) for the details. (B) Parameter dependence of tube morphology. The referenced graph is shown in the upper right. CV: coefficient of variance. See the Materials and Methods (III-vii) for determining the parameter values.

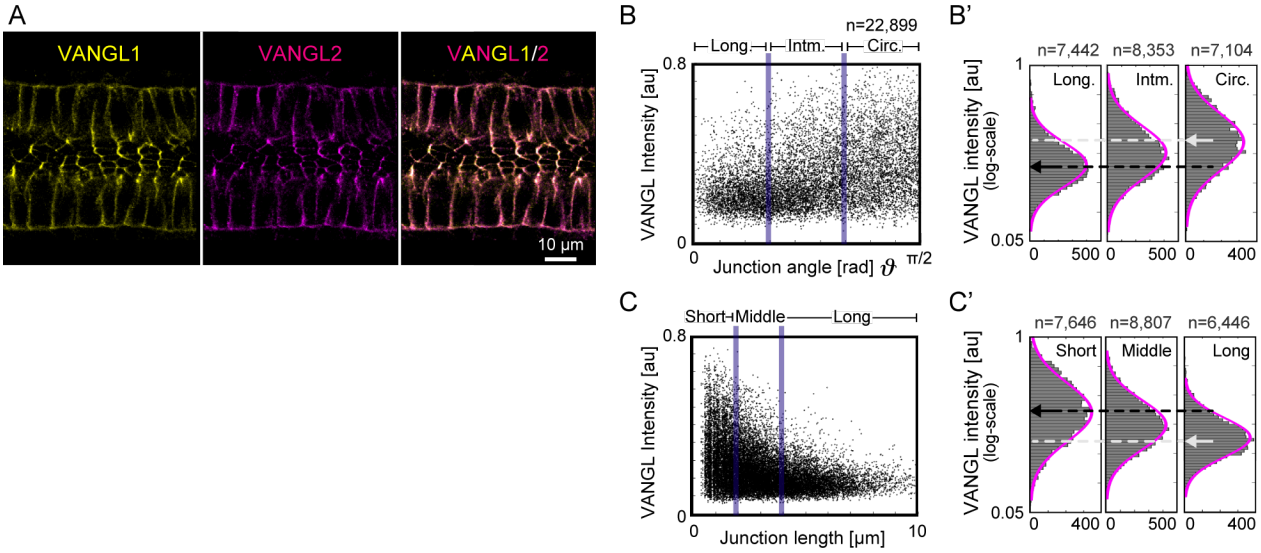

Figure S5 Spatial distribution of polarity proteins Van like protein (VANGL) 1 and 2, corresponding to the Discussion

(A) Immunofluorescence for VANGL1 and VANGL2 demonstrates that their co-localizations are on circumferential junctions of epididymal tubule. (B-C') Relation of junction angle v.s. the fluorescence intensity, and that of junction length v.s. the intensity as with the form of Fig. 3E-F'. These graphs indicate the VANGL localization on the apical junctions of tubule shows significant polarization.

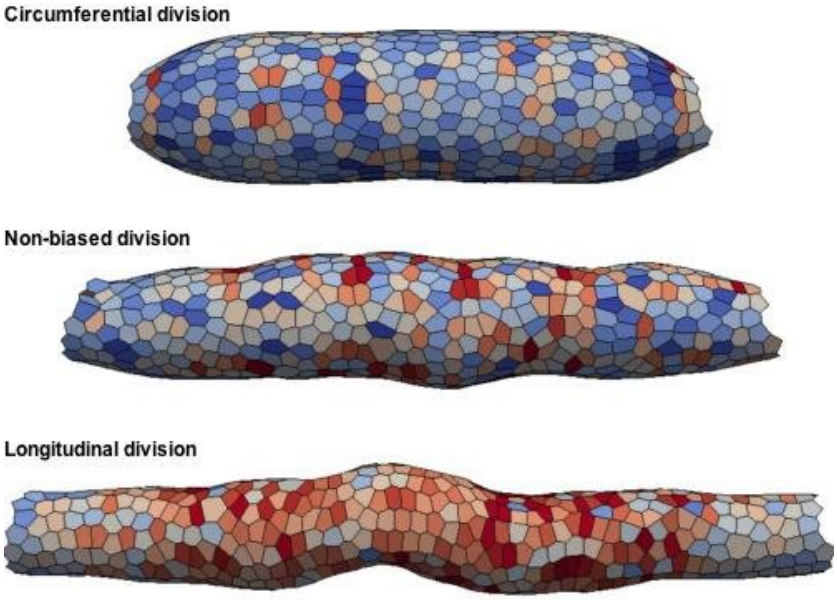

Movie 1 Model Simulation in Different Cell Division Orientation

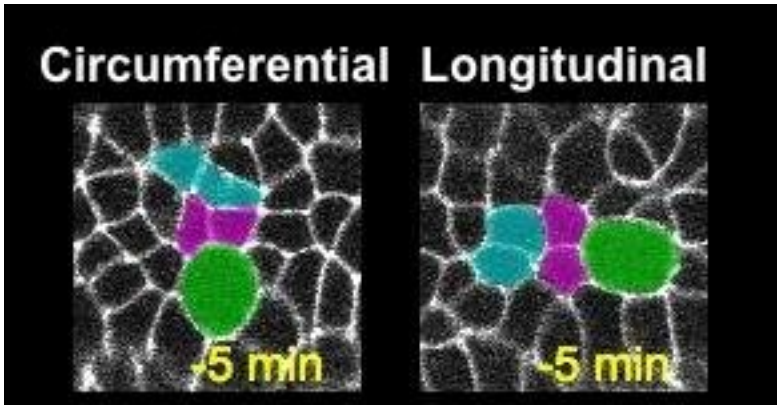

Movie 2 Live Imaging for Multicellular Behaviors against Cell Division

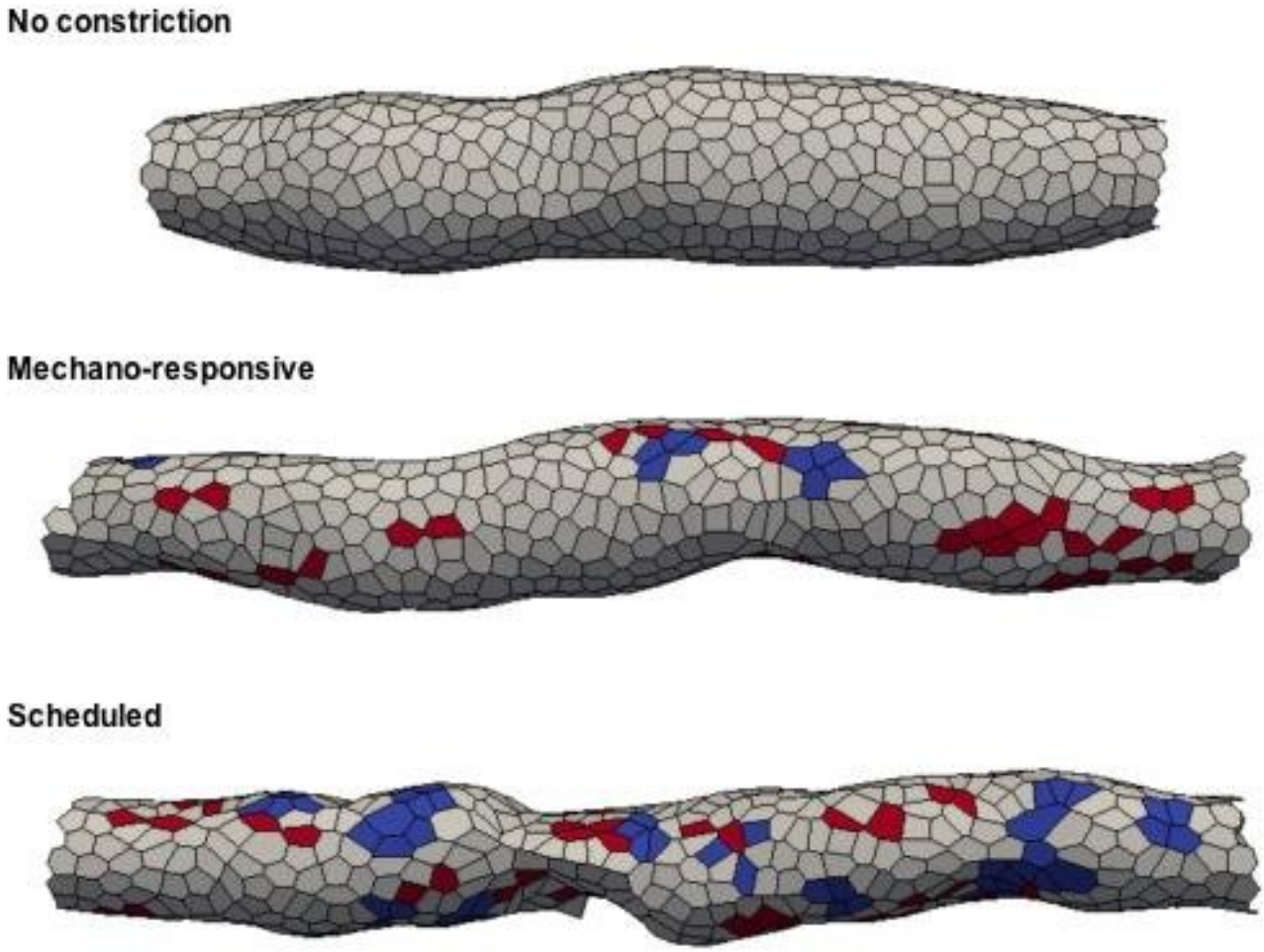

Movie 3 Model Simulation in Different Regimes